Journal of Materials Chemistry C

ROYAL SOCIETY OF CHEMISTRY

PAPER

View Article Online
View Journal | View Issue



Cite this: J. Mater. Chem. C, 2024, 12, 1728



# Trap engineering through chemical doping for ultralong X-ray persistent luminescence and anti-thermal quenching in $Zn_2GeO_4$†

Annu Balhara,[ab] Santosh K. Gupta,*[ab] Malini Abraham,[cd] Brindaban Modak,[be] Subrata Das,[cd] Chandrani Nayak,[f] Harshini V. Annadata[g] and Mohit Tyagi[bh]

Received 13th October 2023,
Accepted 17th December 2023

DOI: 10.1039/d3tc03731b

rsc.li/materials-c

Recently, defect luminescence-based ultralong persistent luminescent (PersL) materials have been increasingly appreciated for advanced applications. However, an in-depth understanding of trap manipulation is a big challenge in controlling trap distribution. In this work, we provide a complete understanding of defect-induced photoluminescence (PL) in $Zn_2GeO_4$ and the significant role of different defects and defect complexes. Excitation-dependent tunable emissions from blue to green regions indicated different mechanisms for filling traps for different excitation energies. Time-resolved emission spectroscopy (TRES) revealed time-dependent trap distribution, shifting the PL band from blue to green. The existence of different electron–hole recombination pathways in different time windows shed light on the complex PL of $Zn_2GeO_4$. Systematic temperature-dependent PL studies imply different trapping and de-trapping processes. We demonstrate the activation energies for different trapping mechanisms and the role of negative thermal expansion (NTE) of $Zn_2GeO_4$ in achieving the negative thermal quenching (NTQ) of PL. Further, the aliovalent doping of $Pr^{3+}$ was used for trap manipulation and introducing additional intermediate defect states. Density functional theory calculations as well as thermoluminescence and electron paramagnetic resonance studies revealed a reduction in defect formation energies for selective defects, four-fold increase in trap density, and trap re-shuffling to optimum trap depths (0.73 eV) on the doping of $Pr^{3+}$. The rich trap distribution resulted in a two-fold increase in the quantum yield of green emissions (~19%) due to Zn interstitial defects. Improved afterglow on UV charging and an increase in the afterglow time from a few minutes in undoped $Zn_2GeO_4$ to an intense X-ray activated afterglow for 18 hours was observed in the $Pr^{3+}$ doped $Zn_2GeO_4$ phosphor. Analysis of afterglow decay kinetics revealed the prominent trap-to-trap tunnelling mechanisms for long lifetimes. Impedance studies revealed the widening of electron channels and reduced resistance to electron movement with the incorporation of $Pr^{3+}$ ions that enhanced PersL. LED fabrication was carried out to demonstrate the potential of the $Zn_2GeO_4$ phosphor for solid-state lighting. We believe that such kinetic and thermodynamic interpretation of defect chemistry will be helpful in tailoring the optoelectronic properties of native defect phosphors.

[a] Radiochemistry Division, Bhabha Atomic Research Centre, Trombay, Mumbai-400085, India. E-mail: santoshg@barc.gov.in, santufrnd@gmail.com
[b] Homi Bhabha National Institute, Anushaktinagar, Mumbai-400094, India
[c] Materials Science and Technology Division, CSIR-National Institute for Interdisciplinary Science and Technology, Thiruvananthapuram, Kerala 695019, India
[d] Academy of Scientific and Innovative Research (AcSIR), Ghaziabad-201002, India
[e] Chemistry Division, Bhabha Atomic Research Centre, Trombay, Mumbai-400085, India
[f] Atomic and Molecular Physics Division, Bhabha Atomic Research Centre, Mumbai-400085, India
[g] Beamline Development & Application Section, Bhabha Atomic Research Centre, Mumbai 400085, India
[h] Technical Physics Division, Bhabha Atomic Research Centre, Trombay, Mumbai-400085, India

† Electronic supplementary information (ESI) available. See DOI: https://doi.org/10.1039/d3tc03731b

## 1. Introduction

Native defect phosphors are an ideal candidate for applications such as solid-state lighting, medical diagnosis, optical tagging, optical storage, photocatalysis and anti-counterfeiting.[1] Over the past decades, native defect phosphors have attracted scientific attention owing to the wide scope for modulating the emission output, photoluminescence quantum yield (PLQY), afterglow, and thermal quenching (TQ) *via* defect engineering.[2,3] In the past, the trap-tuning strategy was investigated in several native defect phosphors to achieve improved PLQY and afterglow.[4] On a broad scale, approaches like doping, synthetic tuning, and band structure engineering have been renowned routes for tuning trap distribution to

attain the desired performance for photocatalysis, electrocatalysis, persistent luminescence (PersL), optical information storage and solid-state lighting applications.[3–9] Particularly, PersL materials with long-lasting afterglow have aroused scientific interest for broad applications, such as emergency lighting, night surveillance, bioimaging, information storage, optical tagging, and photodynamic therapy.[10–12] With the emerging applications of X-ray-activated PersL phosphors in all spheres of mankind, as mentioned above, the quest for understanding the optical phenomenon and afterglow mechanisms stimulated extensive research in this field. However, in-depth investigations need to be conducted on the types of defect states, their behaviour, trapping–detrapping processes, trap distribution, and quenching mechanisms at different excitation wavelengths to develop efficient long PersL materials for targeted applications. Wang *et al.* in their recently published review article have elaborated on the latest developments in $Ce^{3+}$/$Eu^{2+}$-activated phosphors, highlighting the role of correlation between the local structure and photoluminescence (PL) properties to give an overall vision of the composition–structure–property correlations.[13] In recent years, phosphors exhibiting defect-mediated negative thermal quenching (NTQ) of luminescence have demonstrated huge potential for lighting, medical, and security applications owing to the improved thermal stability of emissions.[14,15] Therefore, extensive studies on materials that exhibit defect-related emissions, NTQ, and long PersL are of great importance for establishing a physical correlation between luminescent properties, charge carrier type and trap distribution.

Among the semiconductor oxides, ternary oxide zinc germanate ($Zn_2GeO_4$) has been well established for applications such as display and optoelectronic devices, $CO_2$ photoreduction, water splitting, lithium ion batteries, and ultraviolet (UV) photodetectors.[15–20] $Zn_2GeO_4$ is a wide-band gap oxide ($E_g$ = 4.5 eV) and has received prime attention due to excellent chemical and thermal stability, non-toxicity, self-activated luminescent properties, rich defect density, and high conductivity.[17–19] It is one of the defect-rich phosphors with oxygen vacancies ($V_O^{\bullet}$), zinc interstitials ($Zn_i^{\bullet}$), Zn and Ge vacancies ($V_{Ge}$, $V_{Zn}$) and antisite defects ($Zn_{Ge}$ or $Ge_{Zn}$).[21–23] The white-bluish or green emission under UV excitation is originated from the donor ($V_O^{\bullet}$ and $Zn_i^{\bullet}$)-acceptor ($V_{Ge}$ and $V_{Zn}$) pair (DAP) recombination.[22] Due to diverse applications of $Zn_2GeO_4$, a comprehensive investigation is a prerequisite to correlate the PL and afterglow with the electronic states and intermediate trap levels in $Zn_2GeO_4$. Several reports exhibited the visible emission of $Zn_2GeO_4$ and investigated the spectral changes on doping of $Mn^{2+}$, $Bi^{3+}$, $Yb^{3+}$ and $Li^{+}$ ions.[5,22–24] In our previous work, a detailed experimental and theoretical investigation of PL due to defect states was carried out to realize the PersL blue-green emission of $Zn_2GeO_4$.[23] Recently, Yuan *et al.*[15] have also carried out an in-depth study of negative thermal expansion (NTE) mechanism of $Zn_2GeO_4$ below room temperature (RT). The NTE will result in increased stiffness of the $Zn_2GeO_4$ lattice and can significantly suppress the emission loss due to thermal effects.[25,26] Dolado *et al.*[22] investigated the electronic structure changes, optical output, and NTQ of Li-doped $Zn_2GeO_4$. Some other prominent works explored the bright green PersL in $Mn^{2+}$-doped $Zn_2GeO_4$ phosphors for applications in fluorescence latent fingerprinting, biosensing, and rewritable information storage.[5,27–29] In spite of significant investigations on $Zn_2GeO_4$ phosphors for various applications, the discussion about the origin of photoluminescence, trap distribution, afterglow mechanisms, and trapping–detrapping processes is limited to few studies. Unfortunately, reports on complete mechanistic studies of defect-mediated PL, negative thermal quenching of PL in $Zn_2GeO_4$ phosphors, role of structure rigidity, and different trapping and recombination processes at different excitation wavelengths and temperatures, are missing in the literature. Short-term afterglow and low PLQY of green emission in $Zn_2GeO_4$ phosphors are still the major concerns for real-time applications.

In this regard, the substitution of $Zn^{2+}$ sites by a hyper-valent rare earth ion ($RE^{3+}$) can be a promising approach for introducing additional intermediate defect states and thus modulating the trap depth and probability of DAP transitions.[4] Moreover, the charge mismatch and large ionic radii of $RE^{3+}$ ions will induce energetically favoured formation of $V_{Zn}^{'}$ and $V_O^{\bullet}$ vacancies to retain the charge balance. We judiciously chose $Pr^{3+}$ ion for aliovalent doping in $Zn_2GeO_4$ because $RE^{3+}$ incorporation at $Zn^{2+}$ sites will generate additional electron and hole trap states ($Pr_{Zn}^{\bullet}$ and $V_{Zn}^{'}$) in $Zn_2GeO_4$. The change in trap distribution modulates the trap depths resulting in different trapping–detrapping processes which have profound effect on defect-driven photoluminescence. Gao *et al.*[5] reported the tuning of band gap and trap depths by $Pr^{3+}$ doping. $Pr^{3+}$ doped inorganic materials are a great and highly favorable platform for the realization of longer and more intense persistent luminescence for multifunctional applications. Mao and his group have recently published a review article on various fascinating properties of $Pr^{3+}$ doped phosphors for persistent luminescence and it covers various facets of $Pr^{3+}$ ions.[30] Recently, $Pr^{3+}$ co-doping in $Zn_2GeO_4$:$Mn^{2+}$ phosphor has been reported for enhanced storage photostimulable luminescence (PSL) due to defect engineering.[5] Interestingly, no typical sharp bands of $Pr^{3+}$ ions were observed in the PL and excitation spectrum, suggesting negligible radiative recombination between energy levels of $Pr^{3+}$ in $Zn_2GeO_4$. Wan *et al.* reported similar enhancement in afterglow in $Pr^{3+}$ co-doped $Zn_2GeO_4$:$Mn^{2+}$ and no $Pr^{3+}$ peaks were reported in the emission spectra.[31] Hence, aliovalent doping of $Pr^{3+}$ ions in $Zn_2GeO_4$ can be a promising approach for trap tuning and investigating trapping processes without the interference of $RE^{3+}$ emissions with the host emissions.

Realizing the great potential of self-activated $Zn_2GeO_4$, this work is an effort to investigate the photo-dynamics of defect-related visible emissions of $Zn_2GeO_4$ and understand the nature of DAP recombination resulting in a complex PL band. Temperature-dependent small-angle X-ray diffraction (SAXD) patterns of $Zn_2GeO_4$ were acquired below room temperature and X-ray diffraction (XRD) patterns above RT to investigate the NTE of the $Zn_2GeO_4$ lattice. A doping strategy of aliovalent $Pr^{3+}$ ions is used to trigger defect formation in $Zn_2GeO_4$ and

introduce intermediate energy levels in the bandgap. The effect of $Pr^{3+}$ ion doping in $Zn_2GeO_4$ on the PL properties, PLQY, defect concentration and trap depth, thermal stability and afterglow has been investigated extensively. The possible defect states in undoped and $Pr^{3+}$-doped $Zn_2GeO_4$ systems, along with their defect formation energies, were probed by density functional theory (DFT) calculations. The influence of $Pr^{3+}$ doping on the local structure was revealed by Raman spectroscopy. Synchrotron-based X-ray absorption near edge structure (XANES) and extended X-ray absorption fine structure (EXAFS) measurements were employed to probe the oxidation state of Pr and the local structure of Zn and Ge on Pr doping. DFT calculations were performed to obtain defect formation energies and to probe the formation of intermediate defect states on $Pr^{3+}$ doping. Importantly, we demonstrated the excitation wavelength-dependent tunable emissions in undoped and $Pr^{3+}$ doped $Zn_2GeO_4$. Steady-state and time-resolved emission spectroscopy (TRES) studies were performed for undoped and $Pr^{3+}$ doped $Zn_2GeO_4$ phosphors to understand the decay kinetics of emissions from different excited species. Temperature-dependent PL studies were carried out to explore the NTQ of luminescence in $Zn_2GeO_4$ observed below RT. In-depth investigations on the temperature-dependent PL revealed the activation energies for NTQ and positive thermal quenching (PTQ) processes and different trapping–detrapping mechanisms. Further, the afterglow studies were performed to explore the mechanism involved and the role of $Pr^{3+}$ in the long afterglow decay. X-ray-activated PersL studies were performed, and a long afterglow for $Pr^{3+}$ doped $Zn_2GeO_4$ was captured after ceasing the X-ray excitation. The afterglow property can be a promising approach for reducing the dimming time of phosphor-converted light emitting diodes (pc-LEDs) and hence, we have demonstrated the potential of undoped $Zn_2GeO_4$ and $Pr^{3+}$ doped $Zn_2GeO_4$ phosphors for pc-LEDs. The above insights into trap engineering through aliovalent $Pr^{3+}$ doping in $Zn_2GeO_4$ for tuning the emission, PLQY, and afterglow will help in utilizing $Zn_2GeO_4$ phosphor for potential applications. The material synthesis, instrumentation, details about EXAFS measurements/discussions and computational methodology for DFT calculations are mentioned in the ESI† file as S1, S2, S3, and S4, respectively.

## 2. Results and discussion

### 2.1. Structural, phase, NTE, and local structure analysis

The XRD patterns of undoped $Zn_2GeO_4$ and $Zn_2GeO_4$:$xPr^{3+}$ ($x$ = 0.005, 0.01, 0.02, and 0.05) synthesized by a two-step solid-state route are presented in Fig. 1a. The XRD patterns match completely with the literature (PDF no. 011-0687) that confirmed the formation of rhombohedral structure of $Zn_2GeO_4$ lattice in all the samples. No impurity peaks were observed in the XRD pattern of $Zn_2GeO_4$. However, the introduction of $Pr^{3+}$ ions at higher doping concentrations ($x > 0.01$) resulted in the appearance of extra peaks with weak intensities due to the presence of unreacted $GeO_2$. The crystal structure of $Zn_2GeO_4$ (Fig. 1b) consists of $GeO_4$ and $ZnO_4$ tetrahedra forming four-membered and two different six-membered rings with non-equivalent Zn sites ($Zn_1$ and $Zn_2$).

Raman spectroscopy was performed to study the phase formation and explore the doping effects of $Pr^{3+}$ on the local structures. The peaks in the Raman spectra of $Pr^{3+}$ doped $Zn_2GeO_4$ (Fig. S1a, ESI†) are similar to the Raman spectra of undoped $Zn_2GeO_4$.[23] The peaks at 744 and 801 $cm^{-1}$ are associated with the stretching vibrational modes of $GeO_4$. The Zn–O–Ge stretching and Zn–O–Ge bending modes appeared at 752 and 776 $cm^{-1}$ in the $Zn_2GeO_4$ : 0.01$Pr^{3+}$ (0.01Pr) sample, respectively.[15,23] The wave numbers of the Raman bands were

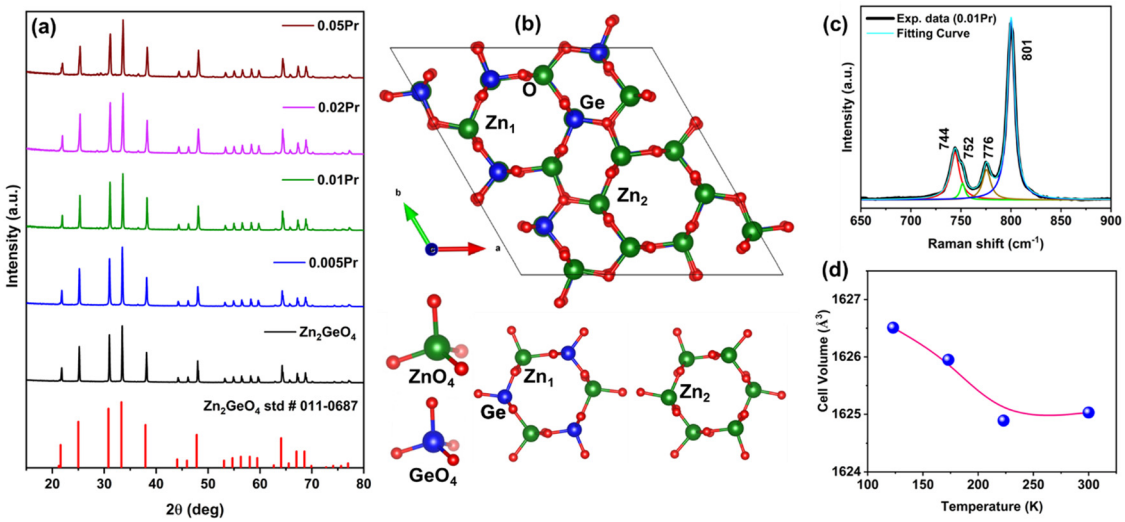


Fig. 1 (a) XRD patterns of $Zn_2GeO_4$:$xPr^{3+}$ ($x$ = 0, 0.005, 0.01, 0.02, and 0.05) samples. (b) Crystal structure of $Zn_2GeO_4$ with $ZnO_4$ and $GeO_4$ tetrahedral units and two non-equivalent Zn sites in six-membered rings. (c) Raman spectrum of the 0.01Pr sample, and (d) cell volume (Å$^3$) of $Zn_2GeO_4$ as a function of temperature in Kelvin.

 

obtained by Lorentzian fitting of Raman spectra (Fig. 1c), and shifts of these Raman bands as a function of $Pr^{3+}$ doping concentrations are displayed in Fig. S1b (ESI†). A blue shift of Raman bands was observed on $Pr^{3+}$ doping at low concentrations ($x \leq 0.01$) followed by a red shift at higher doping concentrations. The blue shifts indicated increased stiffness of $Zn_2GeO_4$ crystal lattice on doping of $Pr^{3+}$ at low concentrations.[15] Fourier transform infrared spectroscopy (FTIR) spectra showed similar patterns in undoped and $Pr^{3+}$ doped $Zn_2GeO_4$ and the characteristic peaks were observed below 800 $cm^{-1}$ (Fig. S2, ESI†). The vibrational modes of the $ZnO_4$ and $GeO_4$ tetrahedra appeared in the range of 400–650 $cm^{-1}$ and 660–850 $cm^{-1}$. The EDS spectra of $Pr^{3+}$ doped phosphors confirmed the presence of Zn, Ge, O, and Pr elements, and elemental mapping indicated homogenous distribution (Fig. S3a–d, ESI†). Further, energy-dispersive X-ray fluorescence (ED-XRF) confirmed the presence of Zn, Ge, and Pr elements in doped samples (Fig. S3e, ESI†).

Temperature-dependent XRD patterns acquired below RT were used to investigate the thermal expansion (TE) behavior of $Zn_2GeO_4$ on heating. The low-temperature SAXD patterns were acquired from 123 to 300 K (Fig. S4, ESI†), and Fig. S5a (ESI†) shows the structure refinement of XRD data taken at 123 K. The lattice parameters of $Zn_2GeO_4$ determined from Rietveld refinement and lattice constants are found to be $a = b = 14.099$ Å, and $c = 9.439$ Å ($\alpha = \beta = 90^\circ$, and $\gamma = 120^\circ$) at RT. The lattice volume contraction or NTE of the $Zn_2GeO_4$ lattice was revealed from the decreased cell volume and cell constants on heating the sample from 123 to 300 K (Fig. 1d). All the three $a$, $b$, and $c$ axes shrink on heating below RT and hence, $Zn_2GeO_4$ exhibit a three-dimensional NTE (Fig. S5b, ESI†). Yuan *et al.*[15] ascribed NTE to the ''external modes'' with low-frequency vibrations and the transverse vibrations of O atoms in $ZnO_4$ and $GeO_4$ tetrahedra forming six and four-membered rings with large spaces. However, $Zn_2GeO_4$ exhibits a very low NTE, resulting in a gradual decrease in the lattice constants and lattice volume below RT. XRD patterns were recorded above RT to study the behaviour of thermal expansion of the $Zn_2GeO_4$ lattice above the RT. XRD peaks shift towards the lower $2\theta$ values on heating the $Zn_2GeO_4$ sample above RT (Fig. S6, ESI†). This confirmed the lattice expansion of $Zn_2GeO_4$ above RT, and thus, the NTE effect is prominent below RT. This suggested that the structural rigidity of the $Zn_2GeO_4$ lattice can efficiently suppress the thermally activated non-radiative transitions up to RT. Further, the low thermal expansion coefficient of the $Zn_2GeO_4$ lattice has attracted attention to investigating the optoelectronic properties of $Zn_2GeO_4$ above RT.

The surface composition of $Zn_2GeO_4$ and 0.01Pr samples and the influence of $Pr^{3+}$ doping on the chemical and structural properties of $Zn_2GeO_4$ were investigated by XPS measurements. The survey scan and XPS spectra of Zn3d (10.7 eV), Zn2p (1022 and 1045 eV), and Ge3d (32.3) confirmed the presence of Zn and Ge in +2 and +4 oxidation states, respectively (Fig. S7, ESI†). The Zn3d, Zn2p, and Ge3d peaks in the Pr-doped $Zn_2GeO_4$ shifted to lower binding energies, which indicated a different chemical environment around these ions in both samples. Ge3d spectra with only a single component can be attributed to the Ge–O bonds in $GeO_4$ tetrahedra. The Gaussian deconvoluted XPS spectra of the O1s peak in undoped and doped samples display two deconvoluted peaks (Fig. S8, ESI†). The former can be ascribed to lattice oxygen, while the latter may have contributions from oxygen vacancies or surface adsorbed oxygen. Moreover, due to a very low concentration of $Pr^{3+}$, XPS does not reveal reliable information on its oxidation state.

The substitution site of large $Pr^{3+}$ ions (0.99Å) in $Zn_2GeO_4$ was unclear as it may substitute $Zn^{2+}$ ions (0.74 Å) or enter the interstitial sites of the six-membered rings. To explore the local structure and oxidation state of Pr ions in $Zn_2GeO_4$, XANES (Fig. S9, ESI†), and EXAFS measurements were carried out for Zn K-edge, Ge K-edge, Pr-$L_3$ edge for undoped and Pr doped samples (Fig. S10, ESI†). The details about the synchrotron beamline, as well as EXAFS and XANES fitting, are discussed in S3 (ESI†). The average bond distances ($R$), coordination numbers ($N$), and disorder (Debye–Waller) factors ($\sigma^2$), which give the mean square fluctuations in the distances, have been used as fitting parameters and listed for Zn K-edge, Ge K-edge, and Pr L3 edge in ESI† (Tables S1–S3), respectively. EXAFS studies revealed that the absorption edges (Fig. S10, ESI†) and the XANES features of the undoped and Pr-doped $Zn_2GeO_4$ samples (Fig S9b, ESI†) are exactly the same at the Ge-K edge, which suggested that Pr doping does not change the effective charge and local environment around Ge cations in $Zn_2GeO_4$. From XANES measurement, it is apparent that Pr cations probably occupy the Zn sites in the $Zn_2GeO_4$ structure. The $\sigma^2$ values increased for Ge–O coordination shells, which suggested increased distortion in the local structure of Ge–O bonds on Pr doping due to a large size mismatch. Fig. S9c (ESI†) shows the Pr $L_3$ edge XANES spectra of the Pr doped $Zn_2GeO_4$ samples along with the $Pr_6O_{11}$ standard where Pr cations exist in a mixed oxidation state of +3 and +4. The peaks at 5971 eV and 5982 eV are characteristic of $Pr^{3+}$ and $Pr^{4+}$ cations.[32,33] The Pr $L_3$ edge XANES spectra of $Pr^{3+}$ doped $Zn_2GeO_4$ samples show a single peak at 5971 eV, suggesting that Pr cations exist in +3 oxidation states in Pr doped samples.

### 2.2. DFT calculations

The computational methodology for the DFT calculations is discussed in ESI† (Section S4.1). The calculated lattice parameters for $Zn_2GeO_4$ ($a = b = 14.51$ Å, and $c = 9.69$ Å) are found to be in good agreement with the experimentally and theoretical calculated values ($a = b = 14.27$ Å, $c = 9.53$ Å). Fig. 2a shows the density of states (DOS) plots for undoped $Zn_2GeO_4$, which indicates that the valence band maximum (VBM) is mainly composed of Zn(d) and O(p) orbitals, while the conduction band minimum (CBM) is hybridized states of Zn(s), Ge(s), and O(p) orbitals. The calculated band gap using PBE0 hybrid functional (4.39 eV) is found to be close to the experimental value ($\sim$4.6 eV) and the reported value in the literature (4.50 eV).

The defect formation energies ($E_f$) for the Pr-doped $Zn_2GeO_4$ in the presence of different defects have been computed using the methodology discussed in ESI† (Section S4.2) and are provided in Table 1. To probe the role of different defects on

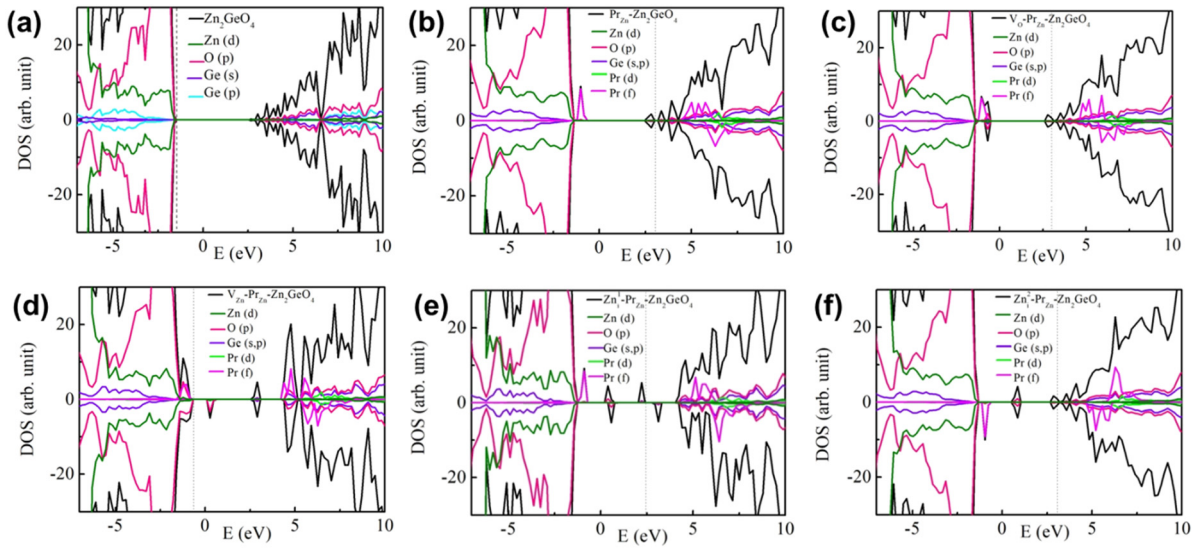


Fig. 2 Density of states for (a) $Zn_2GeO_4$ and (b) $Pr_{Zn}$–$Zn_2GeO_4$ in the presence of (c) one neutral oxygen vacancy, (d) neutral zinc vacancy, (e) zinc interstitial in the Zn–Zn ring position ($(Zn_i^1)$–$Pr_{Zn}$–$Zn_2GeO_4$), and (f) zinc interstitial in the Zn–Ge ring position ($(Zn_i^2)$–$Pr_{Zn}$–$Zn_2GeO_4$).

Table 1 DFT calculated formation energies of defect containing Pr-doped $Zn_2GeO_4$ systems

| System | Defect formation energy (eV) |
|---|---|
| $Pr_{Zn}$–$Zn_2GeO_4$ | −3.33 |
| $V_O$–$Pr_{Zn}$–$Zn_2GeO_4$ | 0.25 |
| $V_{Zn}$–$Pr_{Zn}$–$Zn_2GeO_4$ | 1.02 |
| Zn interstitial ($Zn_i^1$)–$Pr_{Zn}$–$Zn_2GeO_4$ | −1.77 |
| Zn interstitial ($Zn_i^2$)–$Pr_{Zn}$–$Zn_2GeO_4$ | −1.85 |
| Pr interstitial[1] ($Pr_i^1$–$Zn_2GeO_4$) | −1.73 |
| Pr interstitial[2] ($Pr_i^2$–$Zn_2GeO_4$) | −1.61 |

the electronic structure of $Zn_2GeO_4$, we have analyzed the DOS in the presence of different defects. Notably, the $Pr^{3+}$ doping in $Zn_2GeO_4$ may introduce $Pr_{Zn}$ defects when Pr substitutes Zn lattice site and $Pr_i$ defects if $Pr^{3+}$ ions occupy the interstitial sites in six-membered rings. The $E_f$ is the lowest for $Pr^{3+}$ substituting for $Zn^{2+}$, which indicates that the substitutional doping of Pr into the Zn lattice site ($Pr_{Zn}$) is energetically more favourable over interstitial doping ($Pr_i$), which is in line with synchrotron-based X-ray absorption spectroscopy. Herein, we have simulated the $Pr_{Zn}$–$V_O$, $Pr_{Zn}$–$V_{Zn}$ and $Pr_{Zn}$–$Zn_i$ defect complexes to evaluate the $E_f$ and DOS. DFT results revealed that the $Pr_{Zn}$ defects are more energetically favoured than the $Pr_i$ defects.

In our previous work,[23] we calculated the $E_f$ values in undoped $Zn_2GeO_4$ and the formation of $Zn_i$ was found to be the energetically most favourable. Substitution of $Zn^{2+}$ sites by a hyper-valent $Pr^{3+}$ will induce energetically favoured formation of $Pr_{Zn}$ and $V_{Zn}$ vacancies to retain the charge balance. Importantly, the defect complex formation due to the interplay between $Pr_{Zn}$, $V_o$, $Zn_i$, and $V_{Zn}$ defects can effectively alter the defect levels and formation energies. The significant reduction of $E_f$ values on Pr doping in $Zn_2GeO_4$ for all the native defects compared to the $Zn_2GeO_4$ can be attributed to the formation of defect complexes. Impressively, the $E_f$ for $V_o$ decreased from 3.29 eV in undoped $Zn_2GeO_4$ to 0.25 eV for $Pr_{Zn}$–$V_O$ complexes and the $E_f$ for $V_{Zn}$ reduced from 6.35 eV to 1.02 eV on $Pr_{Zn}$–$V_{Zn}$ complex formation. The $E_f$ for the $Zn_i$ defect at both the Zn–Zn and Zn–Ge ring interstitial positions are lowered significantly in the presence of Pr. This indicated that the presence of Pr facilitated the formation of $Zn_i$ defects together with both oxygen and zinc vacancies due to formation of stable defect complexes. Hence, DFT results proposed the increase in defect formation on Pr doping, which will assist in achieving a higher probability of DAP transitions in Pr-doped $Zn_2GeO_4$.

Now, we proceed to investigate the effect of different defects on the electronic structure of $Pr_{Zn}$–$Zn_2GeO_4$. Fig. 2b–f show the DOS for the $Pr_{Zn}$–$Zn_2GeO_4$ unit cell with $Pr_{Zn}$ defects, and $Pr_{Zn}$–$V_O$, $Pr_{Zn}$–$V_{Zn}$, and $Pr_{Zn}$–$Zn_i$ ($Zn_i^1$ and $Zn_i^2$) defect complexes, respectively. We have also investigated the DOS for Pr doping at the interstitial sites and considered two different structures ($Pr_i^1$–$Zn_2GeO_4$ and $Pr_i^2$–$Zn_2GeO_4$) similar to the case of Zn interstitial (Fig. S11, ESI†). Various Pr-dopant-induced energy states were introduced in-between the bandgap due to the presence of $Pr_{Zn}$ defects and formation of different defect complexes. The impurity states induced after Pr doping in $Zn_2GeO_4$ have been discussed in detail in ESI† (Section S4.3) and are displayed in the band edge diagram (Fig. S12, ESI†). Subsequently, the introduction of intermediate levels in the forbidden gap on $Pr^{3+}$ doping in $Zn_2GeO_4$ may result in enhanced optical response of $Zn_2GeO_4$ and the interplay between these defect levels may modulate the afterglow mechanisms.

### 2.3. Photoluminescence studies

The photoluminescence excitation (PLE) and steady-state PL spectra of $Zn_2GeO_4$ under different emission (500 and 535 nm) and excitation wavelengths (265 nm and 310 nm), respectively, are presented in Fig S13a–d (ESI†). $Zn_2GeO_4$ shows a broad bluish-white emission on excitation at 265 nm. The emission of undoped $Zn_2GeO_4$ under ultraviolet (UV) and near-UV (NUV)

 

light could be ascribed to the presence of native defect centers, such as $V_O^{\bullet}$, $Zn_i^{\bullet}$, $V_{Ge}$ and $V_{Zn}$. The $V_O^{\bullet}$ and $Zn_i^{\bullet}$ defects act as the donor centers to trap electrons while $V_{Ge}$ and $V_{Zn}$ act as acceptor centers trapping the holes, and the DAP recombination results in visible emissions. The $Zn_i^{\bullet}$ defects in $Zn_2GeO_4$ are of two types ($Zn_i^1$ and $Zn_i^2$) due to the presence of two different $Zn_i^{\bullet}$ sites in Zn-Zn and Zn-Ge six-member rings, respectively. The bluish-white emission of undoped $Zn_2GeO_4$ under UV excitation has been attributed to DAP recombination.[21,22,24,34,35] In our previous work,[23] the blue-white and green emissions were ascribed to DAP transitions from $V_O^{\bullet}$ and $Zn_i^{\bullet}$ defects introduced in Zn–Zn and Zn–Ge rings, which was supported by DFT calculations. The broad PL in undoped $Zn_2GeO_4$ indicated the complex nature of radiative transitions from different native defects.[36–38] In literature, the assignment of emissions to particular transitions has been controversial due to the competition between conduction bands (CB) to acceptor level transitions and DAP recombination from different donor levels.

Notably, the PLE spectra of undoped $Zn_2GeO_4$ for the emission at 500 nm show an excitation band at 265 nm, while the PLE spectra for 535 nm emission show two excitation bands in the range of 250–290 and 300–345 nm, respectively. The former excitation band can be assigned to the host-related transition (bandgap ~4.67 eV) from the valence band (VB) to CB. The existence of the 310 nm band revealed the direct population of defect energy levels ($V_O^{\bullet}$, $Zn_i^{\bullet}$) between the bandgap *via* excitation with NUV photons.[34,35] The investigation of PL properties of $Zn_2GeO_4$ at band-to-band and below bandgap excitation energies could be helpful to gain insights about the excitation-dependent trap filling and recombination processes. In the past, few studies have investigated the influence of weak excitations on trap distribution and recombinations in materials and revealed the filling of only deep traps under below-band excitations.[39–41]

The NUV excitation band of $Zn_2GeO_4$ observed in our case is rarely reported (Fig. S13b, ESI†). This suggested that a high defect concentration in $Zn_2GeO_4$ phosphors can be achieved *via* a two-step solid state synthetic route used in this work. In our case, a broad visible emission peak at 505 nm was observed on 265 nm excitation comprised of significant contribution from both the $V_O^{\bullet}$ and $Zn_i^{\bullet}$ donor levels to acceptor level DAP recombination along with some probability of CB to deep acceptor level charge-carrier recombination. The appearance of broad visible emissions and less intense UV or NUV emissions supported our hypothesis of a high density of native defects on high-temperature annealing (Fig. S13c, ESI†). This can be explained by fast electron trapping processes by trap states near CB in defect-rich $Zn_2GeO_4$. In earlier work, the prominent presence of strong UV emissions was seen by Dolado and group.[22,34] In contrast, the below bandgap excitation will populate the defect levels selectively, and the radiative transitions from CB do not appear in the PL emission spectra excited at 310 nm as no free electrons will be present in CB. In $Zn_2GeO_4$, the $V_O^{\bullet}$ defects are shallow donors, which can be populated on excitation above bandgap. The PL band became narrow and the percentage of blue and red emissions were decreased under weak excitation. Dolado *et al.*[34] proposed that the radiative charge-carrier recombinations from the $Zn_i^{\bullet}$ related levels are preferred on below bandgap excitation compared to the DAP from the $V_O^{\bullet}$ levels and CB. However, only the UV and NUV bands were considered for the detailed investigation. Our results are consistent with the literature, and hence, we proposed that the visible emissions observed on below bandgap NUV excitations originate mainly from $Zn_i^{\bullet}$ related donor levels in undoped $Zn_2GeO_4$ with insignificant contribution from the CB and $V_O^{\bullet}$ levels. Interestingly, the broad bluish-white emission band observed at 265 nm due to the existence of complex DAP recombinations was transformed into a narrow green emission band under 310 nm excitation. The changes in PL properties due to different trap filling processes led to color tunable emission on different excitations.[23] The conception of the nature of different transitions emitting different visible emissions can be derived from the above observations. The blue emissions are majorly comprised of emissions from CB to acceptor level transitions and DAP transitions from the $V_O^{\bullet}$ donor, the green emissions are majorly from the DAP transitions from two different $Zn_i^{\bullet}$ donors, and the green-yellow emissions are a result of the DAP recombination involving deep donor or acceptor levels. The interactions between $V_O^{\bullet}$ and $Zn_i$ levels may form $V_O^{\bullet} - Zn_i$ defect complexes and result in deep defect levels in bandgap along with the anti-site defects. The bluish-white emission of $Zn_2GeO_4$ under UV excitation with a high PLQY (~42%) can be promising for solid-state lighting applications.[23] However, the low PLQY of green emission (~9%) obtained in undoped $Zn_2GeO_4$ on below band NUV excitation was a major drawback. The green $Zn_2GeO_4$ phosphors excitable with NUV photons and high PLQY would have more potential for LED applications.

Aiming at tailoring the trap distribution, we carried out $Pr^{3+}$ doping in $Zn_2GeO_4$. The defect formation on the substitution of two $Zn^{2+}$ ions by two $Pr^{3+}$ ions and three $Zn^{2+}$ ions by two $Pr^{3+}$ ions in the case of low and high doping concentrations can be explained with the help of Kröger–Vink notations by the following processes:[35]

$$2Pr^{3+} \rightarrow 2Zn^{2+} + V_O^{\bullet\bullet} \quad (1)$$

$$V_O^{\bullet\bullet} + e^- \rightarrow V_O^{\bullet} \quad (2)$$

$$2Pr^{3+} + 3Zn^{2+} \rightarrow 2Pr_{Zn}^{\bullet} + V_{Zn}'' \quad (3)$$

$$V_{Zn}'' \rightarrow V_{Zn}' + e^- \quad (4)$$

Additionally, the distortion in the [$GeO_4$] and [$ZnO_4$] local structure endowed by both size and charge mismatch on $Pr^{3+}$ aliovalent doping further boosted the formation of $Zn_i^{\bullet}$ and $V_{Ge}$. The increased defect formation may improve the defect emissions as DAP recombinations would be enhanced on $Pr^{3+}$ doping.

The PLE and PL emission spectra of all the $Pr^{3+}$ doped samples were recorded under the 265 nm excitation and below

bandgap (310 nm) excitation energies (Fig. S14 and S15, ESI†). The $Pr^{3+}$ doped samples show a broad emission band peak at 535 nm when excited at 265 nm. A small doping concentration of $Pr^{3+}$ ($x$ = 0.005) resulted in decreased PL intensity, but a subsequent increase was observed when the $Pr^{3+}$ doping concentration was increased up to 0.01. The intensity decreased on further increase in the doping concentration (>0.01) as a consequence of concentration quenching. In addition to DAP recombinations, the probability of a weak energy transfer (ET) from the host to $Pr^{3+}$ ions could not be ruled out. In our case, no sharp emission peaks for f → f transitions of $Pr^{3+}$ ions were observed in any of the $Pr^{3+}$ doped samples. This revealed the absence of efficient radiative transitions between 4f levels of $Pr^{3+}$ ions in the $Zn_2GeO_4$ host. Similar observations have been reported in $Pr^{3+}$ doped $Zn_2GeO_4$:$Mn^{2+}$.[5,31] He *et al.*[35] have reported a weak ET from $Zn_2GeO_4$ host to $Eu^{3+}$ ions resulting in defect-dominated emission along with less intense $Eu^{3+}$ emissions. Based on the above observations, the 0.01Pr sample with an optimum concentration of $Pr^{3+}$ ($x$ = 0.01) was considered for the comparative investigation of the doping effect on PL, defect distribution, and optoelectronic properties with respect to $Zn_2GeO_4$.

It can be observed from the excitation spectra of undoped and 0.01Pr phosphors (Fig. 3a) that the 0.01Pr exhibited an intense shoulder absorption band when emission was monitored at both the 500 and 535 nm. This can be explained by the DFT results, which revealed that $Pr^{3+}$ doping introduced various additional defect states between the VB and CB. The 0.01Pr phosphor is rich in midgap defect states and impurity levels, and broad PLE spectra can be attributed to the direct activation of these levels by UV light. Subsequently, the probability of electron excitation in CB is inappreciable in 0.01Pr phosphor, and probably, only the defect states would be populated even on bandgap excitation (265 nm). The normalized emission spectra of undoped and 0.01Pr samples excited at 265 nm (Fig. 3b) demonstrated a red shift in the emission peak on $Pr^{3+}$ doping from 500 to 535 nm, and a slightly resolved emission spectra could be observed in the $Pr^{3+}$ doped samples. This suggested that $Pr^{3+}$ doping prompted the DAP transitions, resulting in green emissions more selectively. Consequently, the blue emissions became less intense as no free electrons were available in CB for CB-acceptor level transitions. Clearly, below bandgap NUV excitations (310 nm) also contributed to the final green emission in $Pr^{3+}$ doped samples. In $Pr^{3+}$ doped $Zn_2GeO_4$, weak below bandgap excitations can populate the donor levels *via* excitations from VB or acceptor levels, and the PL emission will be solely due to DAP transitions. In our

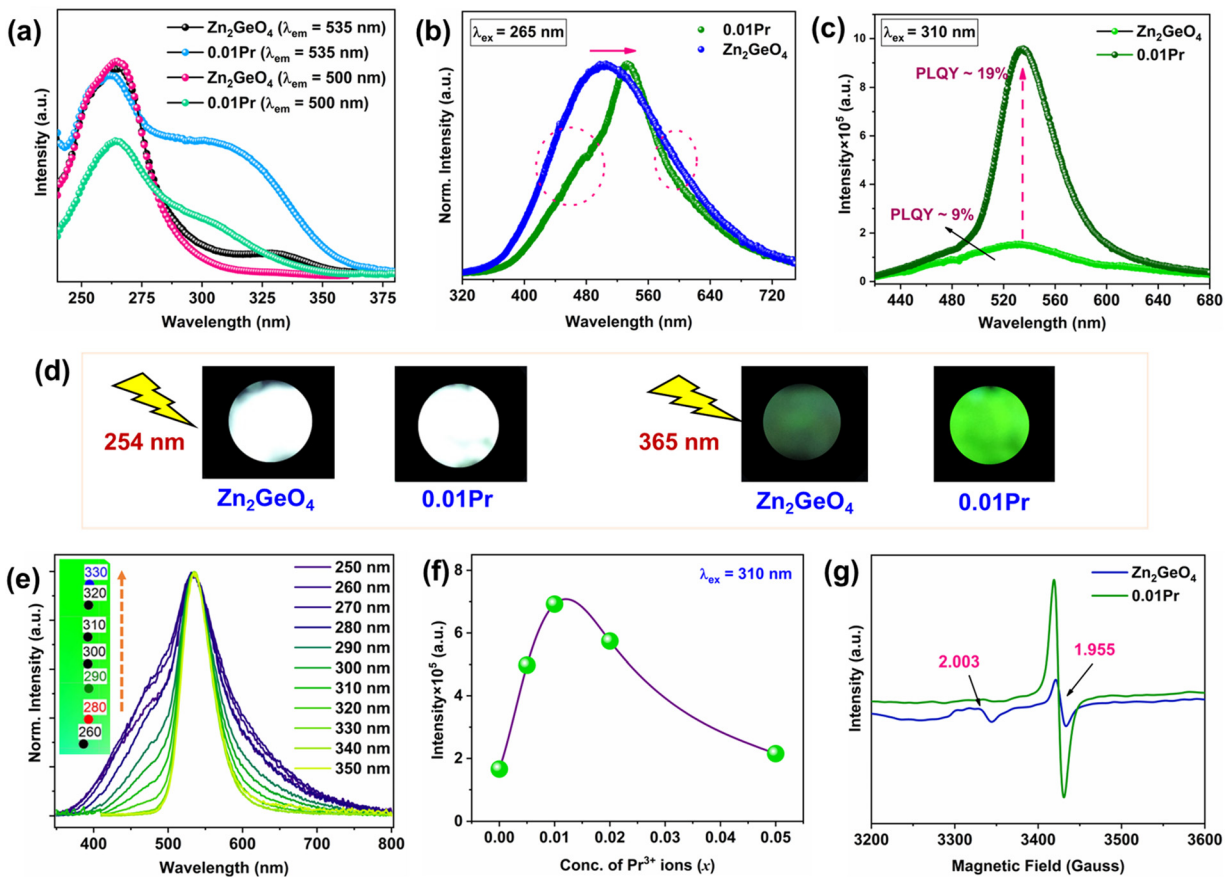


Fig. 3 (a) PLE spectra of undoped and 0.01Pr samples at different emission wavelengths, (b) and (c) PL spectra of undoped and 0.01Pr sample at 265 nm and 310 nm excitation, respectively. (d) Emission photographs captured by a Nikon camera under 254 and 365 nm UV lamp. (e) Emission spectra of 0.01Pr at different excitation wavelengths. (f) Green emission intensity changes as a function of $Pr^{3+}$ doping concentrations, and (g) EPR spectra of $Zn_2GeO_4$ and 0.01Pr samples at 100 K.

 

interest, a remarkable four-fold enhancement in the intensity of the green emission band peaking at 535 nm on $Pr^{3+}$ doping under excitation at 310 nm is seen (Fig. 3c). We kept the samples in air for a month and tested the stability of our material by monitoring the optical properties at regular intervals. We recorded the emission spectra of the samples on the 1st, 5th, 15th, and 30th day. No significant decrease in photoluminescence output was observed in the samples. The same has been provided in the ESI† file as Fig. S16.

To visualize the color tunability of emissions on $Pr^{3+}$ doping in $Zn_2GeO_4$, the emission images of samples under a UV lamp at 254 and 365 nm are shown in Fig. 3d and CIE color coordinate diagrams are provided as Fig. S17a and b (ESI†). The excitation-dependent PL emission spectra of 0.01Pr display color tunability due to different trapping mechanisms at different excitation energies (Fig. 3e and Fig. S18, ESI†). The increase in the excitation wavelength from 250 to 350 nm decreased the full width at half maximum (FWHM) of emission spectra. At higher excitation energies, the broad visible emission was observed, which is supposed to have a significant contribution from both the $V_O^{\bullet}$ and $Zn_i^{\bullet}$ donor levels to acceptor level DAP recombinations and charge carrier recombinations from CB to deep acceptor levels. In contrast, the below bandgap excitations may populate the defect levels selectively, and the probability of radiative transitions from CB is negligible as no free electrons will be present in CB due to higher concentrations of intermediate defect states. Hence, the PL emission band became narrow as it comprised only DAP recombinations from the $V_O^{\bullet}$ and $Zn_i^{\bullet}$ donor levels.

To illustrate the effect of $Pr^{3+}$ doping in the green emissions, the intensity changes as a function of $Pr^{3+}$ doping concentrations are shown in Fig. 3f. A two-fold increase in the PLQY ($\sim$19%) of green emission under NUV excitation was attained on $Pr^{3+}$ doping in $Zn_2GeO_4$ (Fig. S19, ESI†). The increased green emission can be explained by DFT results, indicating that $Pr^{3+}$ doping will facilitate the formation of $Pr_{Zn}^{\bullet}$ and $Zn_i$ defect-related levels, which can act as electron traps and $V_{Zn}$ as hole traps. The high $E_f$ of $V_{Zn}$ reported for undoped $Zn_2GeO_4$ suggested that the formation of $V_O$ and $Zn_i$ defects is more favourable than $V_{Zn}$.[23] On $Pr^{3+}$ doping, an appreciable reduction in the $E_f$ of $V_{Zn}$ was revealed by theoretical calculations due to the formation of $V_{Zn}$–$Pr_{Zn}$ defect complexes. The increased DAP transitions from $Zn_i^{\bullet}$ related donor levels to $V_{Zn}^{'}$ acceptor levels became more prominent on $Pr^{3+}$ doping, which explained the enhanced green emission in $Pr^{3+}$ doped $Zn_2GeO_4$.

EPR measurements of undoped and $Pr^{3+}$ doped $Zn_2GeO_4$ samples were carried out at 100 K to understand the types of native defects (Fig. 3g). The EPR signal at $g \sim 1.955$ is composed of paramagnetic $Zn_i^{\bullet}$ and $V_O^{\bullet}$ defects. The signal at $g \sim 2.003$ is usually reported to $V_O^{\bullet}$ in most of the host matrices.[42] However, the presence of this signal in $Zn_2GeO_4$ can be proposed due to $Zn_i^{\bullet} - V_O^{\bullet}$ defect complex formation or isolated cation vacancies ($V_{Zn}^{'}$).[43–46] The intensity of the EPR signal due to $Zn_i^{\bullet}$ and $V_O^{\bullet}$ defects ($g \sim 1.955$) enhanced significantly in 0.01Pr samples that indicated large defect formation on $Pr^{3+}$ doping. This observation is in line with DFT calculations and also supports the PL results.

Based on the previous literature and our experimental and theoretical results, we proposed an energy band model (Fig. 4a) and respective transitions involving the defect states, which resulted in the broad visible PL of $Zn_2GeO_4$. The luminescence decay profiles of $Zn_2GeO_4$ and 0.01Pr phosphors excited at 265 and 310 nm and emissions monitored at 500 and 535 nm are shown in Fig. S20a and b (ESI†). The decay curves were best fitted with a three-exponential decay function:

$$I(t) = I_0 + A_1 e^{-t/\tau_1} + A_2 e^{-t/\tau_2} + A_3 e^{-t/\tau_3} \quad (5)$$

where $I(t)$ and $I_0$ denote the UC emission intensities at time '$t$' and at zero offset, $A_1$, $A_2$, and $A_3$ are constants, and $\tau_1$, $\tau_2$, and $\tau_3$ are the three lifetime constants, respectively. The lifetime values of $Zn_2GeO_4$ and 0.01 Pr phosphors are summarized in Table S4 (ESI†). The multi-exponential decay can be explained by the presence of different recombination pathways for visible emissions. The short lifetimes are observed due to direct radiative recombinations while the long lifetimes indicated charge trapping in deep traps. The long tail in the decay profiles was observed due to the indirect population of the luminescent sites through tunnelling of carriers from stable non-radiative traps.[47,48]

To further understand the decay kinetics, TRES of $Zn_2GeO_4$ and 0.01Pr phosphors were acquired with the integration time of 200 ms at different delay times in the range of 100 μs to 180 ms (Fig. S21a and c, ESI†). TRES studies can be helpful in resolving overlapping emissions originating from different electron–hole recombinations involving CB, defect states, and VB. At small delay times, all the emission components due to different excited species are supposed to be present, as the lifetime values for visible emissions of undoped and doped $Zn_2GeO_4$ are $>1$ ms (Table S4, ESI†). The normalized TRES spectra at different delay times for $Zn_2GeO_4$ and 0.01Pr phosphors under 265 nm excitation are provided in Fig. 4b and c. In the beginning, the TRES spectra of $Zn_2GeO_4$ excited at 265 nm consisted of a significant contribution from weak NUV emissions along with visible emissions up to a delay time of 100 μs. The NUV and blue emissions decayed faster, and the intensity decreased significantly on longer delay times ($>$100 μs). The same can be visualized by a change in color coordinates of emission from blue towards the blue-green region on increasing delay times (Fig. 4b and Fig. S21b, ESI†). In the case of $Pr^{3+}$ doped $Zn_2GeO_4$, a broad emission consisting of all emissions was observed at a 100 μs delay time and emission components became more resolved on an increase in delay times (Fig. 4c). The TRES of the 0.01Pr sample suggested that the green emissions have longer decay times compared to blue emissions and only green emissions could be observed at longer delay times (Fig. S21c and d, ESI†). The TRES studies of the 0.01Pr sample at below bandgap excitation (310 nm) displayed similar behaviour and showed individual green emissions on long delay times $>$ 300 μs (Fig. S22, ESI†).

Such long decay times (in ms scale) can be explained by charge carrier redistribution in defect states due to the involvement of trap-to-trap tunnelling (or hopping) processes.[41,47,49] The excited electrons in CB and defect states can directly

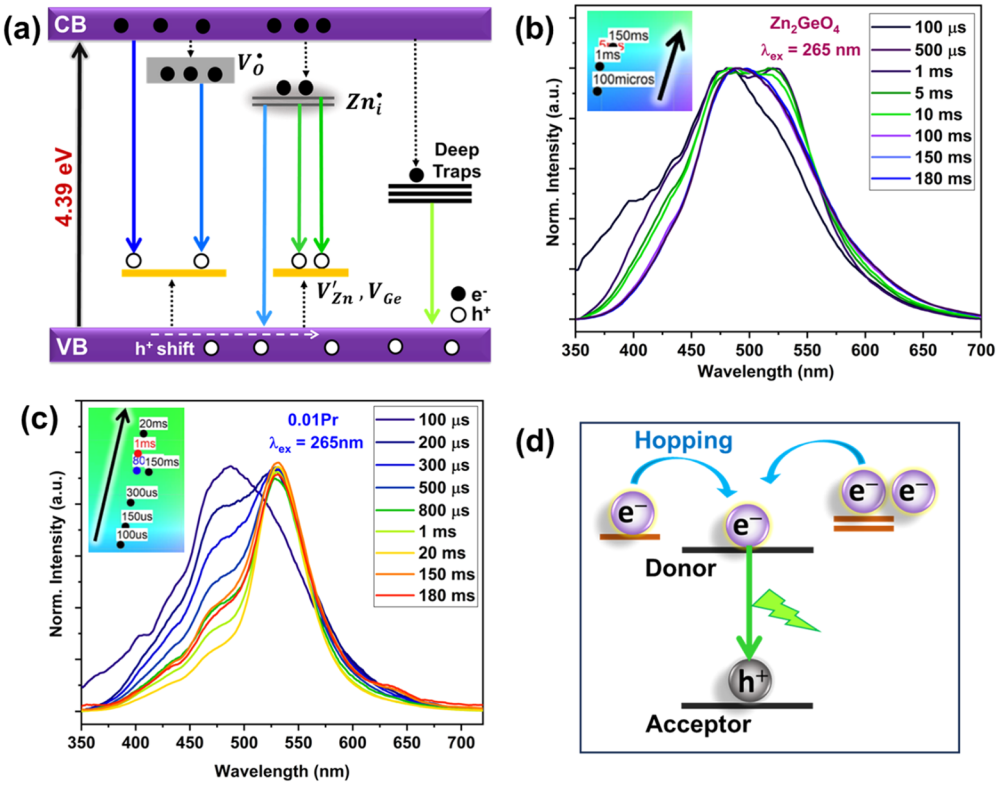


Fig. 4 (a) Energy band diagram demonstrating radiative transitions and DAP recombinations for visible emissions in $Zn_2GeO_4$. Normalized TRES at different delay times of 100 µs to 180 ms for (b) $Zn_2GeO_4$ and (c) 0.01Pr samples. (d) Schematic for the trap-to-trap hopping mechanism.

undergo emissive electron–hole recombinations with short decay times (~µs) or photogenerated carriers may be trapped in stable non-radiative defects. With time, the captured carriers relax *via* tunnelling towards the luminescent sites, which is followed by the visible emissions due to DAP recombinations with a longer time component (~ms) (schematic shown in Fig. 4d). The TRES supported the proposed hypothesis that the blue emissions have contributions from CB and defect states while the green emission bands originated solely from DAP transitions of charge carriers in defect levels. The TRES provided strong evidence for spatial correlation between $Pr_{Zn}^{\bullet}$-induced traps and emissive donor defect centres. Therefore, the 0.01Pr sample exhibits a time-dependent trap distribution due to high trap density in the vicinity of emissive levels that facilitated hopping mechanisms.

### 2.4. Persistent luminescence and Thermoluminescence (TL) studies

To better understand the trapping and de-trapping processes, the PersL decay curves were measured on irradiation of $Zn_2GeO_4$ and 0.01Pr phosphors with UV lamps at 265 and 310 nm, respectively (Fig. S23, ESI†). The afterglow decay curves measured at 265 nm charging for blue-white emissions are shown in Fig. 5a. The afterglow decay curves monitored at 535 nm for the green emission band on charging the phosphors at 310 nm for 100 s are shown in Fig. 5b. For both the excitations, the afterglow intensity was improved on $Pr^{3+}$ doping in $Zn_2GeO_4$. To further explore the mechanisms of decay processes, the experimental afterglow curves were fitted into the power-law exponent function ($\propto t^{-\alpha}$) (Fig. 5a and b). By fitting, the power-law exponent ($\alpha$) was found to be approximately in the range of 0.56–1.06. This behavior is consistent with the TRES findings and lifetime decay observations which suggested that the visible emissions are controlled by the tunnelling of charge carriers between trap states.[41,47,48] On excitation, electrons and holes are captured by traps with some probability of filling charge carriers in stable non-luminous sites. The tunneling of charge carriers in non-luminescent traps populate luminescent defect sites, and are responsible for long afterglow. The schematic illustration for the PersL mechanism is presented in Fig. S24 (ESI†). To calculate the afterglow decay times ($\tau$), the decay curves were fitted with eqn (5) and the $\tau$ values are tabulated in Table S5 (ESI†). It was observed that the afterglow decay times increased on $Pr^{3+}$ doping when the samples were charged at bandgap excitation (265 nm). However, for the 0.01Pr phosphor charged at a below bandgap excitation (310 nm), the $\tau$ values were lower compared to the undoped sample. This can be explained by excitation wavelength-dependent charge distribution in traps.[40] Hence, it can be inferred that the tunnelling processes are dominant at higher excitation energies, resulting in photogenerated carriers with more energy. The migration tendency is higher, which increases the probability of trapping at non-radiative states.[41] The effective filling of charge carriers in all trap

 

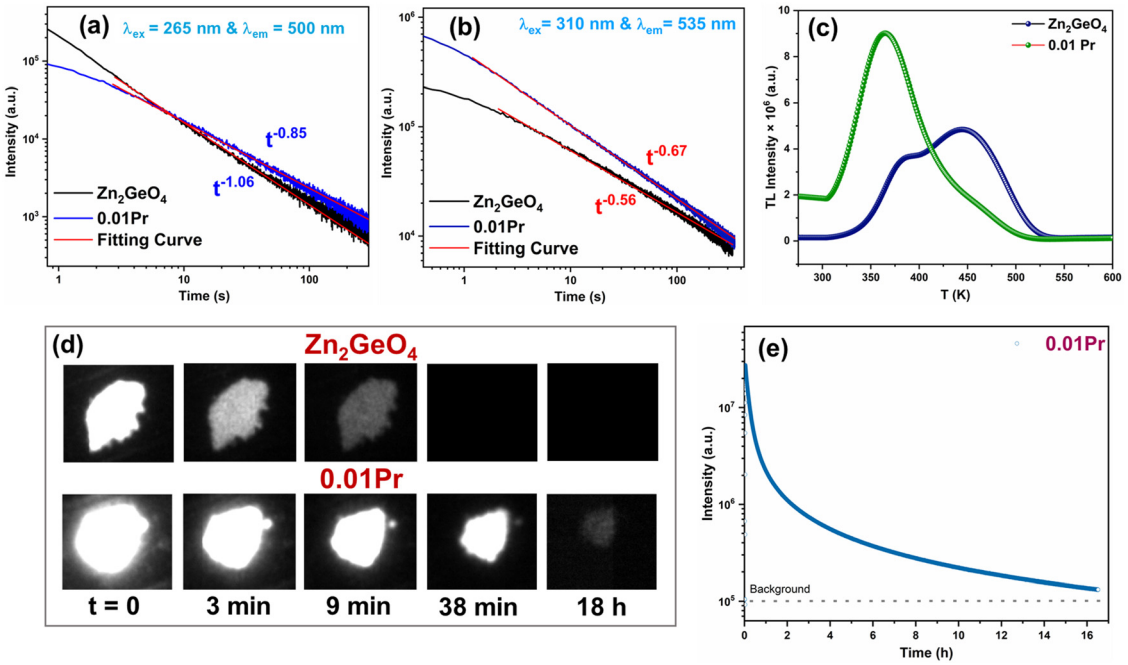


Fig. 5 PersL decay curves of $Zn_2GeO_4$ and 0.01Pr phosphors irradiated at (a) 265 nm and (b) 310 nm for 100 s (the red lines are the fitting of decay with power-law exponent function). (c) TL glow curves for $Zn_2GeO_4$ and 0.01Pr phosphors recorded in the range of 273–600 K on charging at 265 nm for 100 s. (d) X-ray activated PersL images recorded by camera at different time intervals, and (e) X-ray activated PersL decay curve for the 0.01Pr sample.

states can be achieved by increasing the excitation energies. The feasibility of the same was explored with higher energy X-ray excitations to attain long PersL.

TSL studies were performed to reveal the features of trap states, trap depth, and distribution.[9] Fig. 5c depicts the TL glow curves of $Zn_2GeO_4$ and 0.01Pr phosphors after charging by UV irradiation at 265 nm for 100 s. The broad TL emissions on heating of phosphors confirmed the large defect formation in the samples. Two and three components in the TL curves were obtained for $Zn_2GeO_4$ and 0.01Pr samples by Gaussian deconvolution shown in Fig. S25 (ESI†). The trap depth ($E_t$) can be estimated with the help of the following equation:[9]

$$E_t = T_m/500 \quad (6)$$

where $T_m$ is the peak temperature in Kelvin. The calculated $E_t$ values for $Zn_2GeO_4$ for lower and higher temperature TL peaks are 0.77 and 0.90 eV, respectively. The two trap depths deciphered the presence of large shallow and deep trap levels between VB and CB. Interestingly, the TL intensity of low temperatures peak for the 0.01Pr sample increased by nearly 4 times the intensity observed in undoped phosphor (Fig. 5c). This suggested that the $Pr^{3+}$ doping introduced a large number of additional traps, which correlate well with the DFT and EPR results. In the $Pr^{3+}$ doped phosphor, the three TL peaks were observed at a trap depth of 0.55, 0.73, and 0.85 eV, respectively, as the TL peaks shifted towards lower temperatures centered at 279, 363, and 428 K. The increased intensity of shallow traps (~0.55 eV) explained the intense afterglow of the 0.01Pr phosphor at RT. Moreover, the trap depths in 0.01Pr (~0.73 eV) fall in the optimum trap depth range (0.65–0.75 eV) for obtaining an efficient PersL at room temperature.[48] Hence, the enhanced afterglow intensity can be ascribed to the formation of traps with optimum trap depths, as charge carriers captured by deep traps (>0.85 eV) could not escape at room temperature.

In order to understand the effect of different excitations on the trap depth and distribution, the comparison of TL glow curves upon charging the samples with 265 and 310 nm has been provided in Fig. S26a (ESI†). Upon charging with 310 nm, TL glow curves are similar for undoped and 0.01Pr samples, but the TL intensity is significantly higher for 0.01Pr. This indicated a much more effective trap filling in the $Pr^{3+}$ doped sample that resulted in enhanced PersL on charging with 310 nm. The samples irradiated with higher excitation energy (265 nm) resulted in intense TL, which indicated more efficient trap filling as compared to 310 nm. It can be inferred that higher excitation energy can fill a higher concentration of traps, leading to long PersL. However, the filling of relatively shallow traps upon 310 nm charging resulted in intense PersL at room temperature with a shorter afterglow time. The TL glow curves on X-ray irradiation of undoped and 0.01Pr samples, shown in Fig. S26b (ESI†), revealed a much higher concentration of filled traps in the $Pr^{3+}$ doped sample with a rich trap distribution. The broad TL of 0.01Pr explained the long PersL obtained on $Pr^{3+}$ doping due to the slow release of charge carriers from multiple trap states on gaining thermal energy during the afterglow phenomenon.

To explore the PersL on charging the phosphors with higher excitation energy, the $Zn_2GeO_4$ and 0.01Pr phosphors were irradiated with X-rays for 1 min and the PersL intensities were captured by a camera at different decay instants after ceasing

X-ray excitation (Fig. 5d). The radioluminescence (RL) spectra of undoped and $Zn_2GeO_4$:0.01Pr samples are provided in the ESI† file as Fig. S27. The 0.01Pr sample showed intense RL compared to the undoped sample, and the spectral features on X-ray excitation were similar to UV excitation. The 0.01Pr sample displayed an intense X-ray-activated PersL, which could be observed for 18 hours in the dark, while PersL in undoped $Zn_2GeO_4$ completely ceased after 38 min. The X-ray-activated PersL decay curve for the 0.01Pr sample is presented in Fig. 5e. The long PersL decay times of 0.01Pr can be ascribed to prominent tunnelling mechanisms as the PersL decay curve can be well fitted into a power-law exponent function with $\alpha = 1.02$ (Fig. S28, ESI†). The RL afterglow curve for the 0.01Pr sample after ceasing off the X-ray light is provided in Fig. S27b (ESI†), and the decrease in FWHM of RL can be attributed to different de-trapping processes as a function of time. Moreover, the additional defect states introduced on $Pr^{3+}$ doping increased the defect density significantly, as revealed by TL, EPR and DFT studies. The high energy X-ray excitations can result in the distribution of photogenerated charge carriers in all the trap states.[50] Thus, the long PersL in $Zn_2GeO_4$ could be achieved by tailoring the defect states in between the bandgap by doping.

Table S6 (ESI†) lists some of the recent X-ray persistent phosphors and compares their performance with $ZnGe_2O_4$ and 0.01 Pr. Based on this table (Table S6, ESI†), we could find that for some of the phosphors, X-ray persistent luminescence duration was more than 18 h, but they are reported for ultraviolet-B (UVB)/UVC emission and that too in fluoride-based hosts. In both ways, their usability is quite curtailed for commercial lighting owing to non-visible light production and the use of toxic and corrosive fluoride-based hosts. There are two very recent review articles on X-ray persistent phosphors, which can be referred and may be quite useful for new researchers.[51,52] In terms of UV persistent phosphors, $Zn_2GeO_4$ and 0.01Pr phosphors were inferior to some of the recent long afterglow lead halide perovskite materials.[53,54] But the 0.01Pr phosphor excels because it demonstrated remarkable enhancement in X-ray persistent luminescence for more than 18 h with very high radioluminescence intensity.

### 2.5. AC impedance analysis

Decay kinetics suggested the role of tunnelling of charge carriers between trap states in longer afterglow times. To further support the same, the electrochemical impedance (EIS) of $Zn_2GeO_4$ was analysed before and after $Pr^{3+}$ doping. From the impedance curves shown in Fig. S29 (ESI†), it can be observed that the impedance of the $Zn_2GeO_4$ sample reduced on $Pr^{3+}$ doping. The radius of curvature of the 0.01Pr curve decreased compared to the undoped $Zn_2GeO_4$ curve. The impedance drop in $Zn_2GeO_4$ with the incorporation of $Pr^{3+}$ ions revealed the widening of electron channels, which, in turn,[55] reduced the resistance to electron movement in the 0.01Pr phosphor. Hence, the increased electron migration rate in the 0.01Pr sample resulted in enhanced afterglow performance.

### 2.6. Temperature-dependent PL studies

To explore the variation in the defect-related emission of $Zn_2GeO_4$ as a function of temperature, the temperature-dependent PL spectra of $Zn_2GeO_4$ and 0.01Pr phosphors were acquired from 80 to 300 K under excitation at 265 nm (Fig. 6a). It was observed that PL intensity increased on increasing the temperature that revealed the abnormal NTQ of PL in $Zn_2GeO_4$ below RT. The 0.01Pr phosphor (Fig. 6b) exhibited the thermally enhanced PL as the emission intensity increased on increasing the temperature, demonstrating the NTQ effect in doped $Zn_2GeO_4$ as well. Among the various competitive processes, multi-phonon assisted crossover and non-radiative relaxation are one of the mechanisms for thermal quenching.[56] Hence, the NTE effect of $Zn_2GeO_4$ can be one of the reasons for the observed NTQ behavior below RT due to the enhanced structural rigidity of the $Zn_2GeO_4$ lattice up to RT. Liu *et al.* demonstrated the improved thermal stability of luminescence by controlling the structural rigidity.[25] The insignificant non-radiative relaxations due to low-frequency phonon modes in $Zn_2GeO_4$ can efficiently reduce the thermal quenching. At 80 K, well-resolved PL spectra could be observed, while on heating, the emission band became broader with a gradual blue shift. This shift can be explained by the existence of charge trapping in defects, and the population of these defect states varies with temperature.[22] In $Zn_2GeO_4$, the intensity at 300 K is enhanced by 362% of the intensity observed at 80 K (Fig. S30, ESI†).

As mentioned earlier, the emissions under below band gap excitations originate from defect-related DAP transitions. In order to have a clear picture of trap distribution and changes in PL features under low energy excitations, temperature-dependent PL measurements of $Zn_2GeO_4$ and 0.01Pr phosphors were performed from 80 to 300 K under NUV excitation (310 nm). Surprisingly, the PL emissions in $Zn_2GeO_4$ exhibited a completely opposite behavior under below bandgap NUV excitation (Fig. 6c). A normal PTQ of green emission band was observed on weak excitation that resulted in a continuous decrease of PL intensity from 80 to 300 K. The temperature-dependent PL in $Zn_2GeO_4$ displayed divergent NTQ and PTQ processes below RT, which indicated the existence of different activation barriers, trapping and detrapping processes under high (265 nm) and weak excitation energies (310 nm). The temperature-dependent PL of the $Pr^{3+}$ doped $Zn_2GeO_4$ phosphor on below band NUV excitations showed exciting results (Fig. 6d). $Pr^{3+}$ doping resulted in the thermal stability of the green emission of $Zn_2GeO_4$ up to 180 K, followed by a gradual NTQ of PL up to 220 K. A normal PTQ trend was observed on further increase in temperature ($>220$ K). The thermal stability of the green PL band in 0.01Pr phosphors can be explained as a result of a balance between the thermal activation of DAP transitions and thermal quenching. The intensity variation of PL as a function of temperature in undoped $Zn_2GeO_4$ and 0.01Pr phosphors can be visualized in the contour plots in Fig. 6e and f under 265 and 310 nm excitations, respectively. The thermal stability of the green band in $Pr^{3+}$ doped phosphor can be clearly seen in Fig. 6f as the luminous intensity remains almost constant. The PL intensity at 300 K in 0.01Pr was 85% of

 

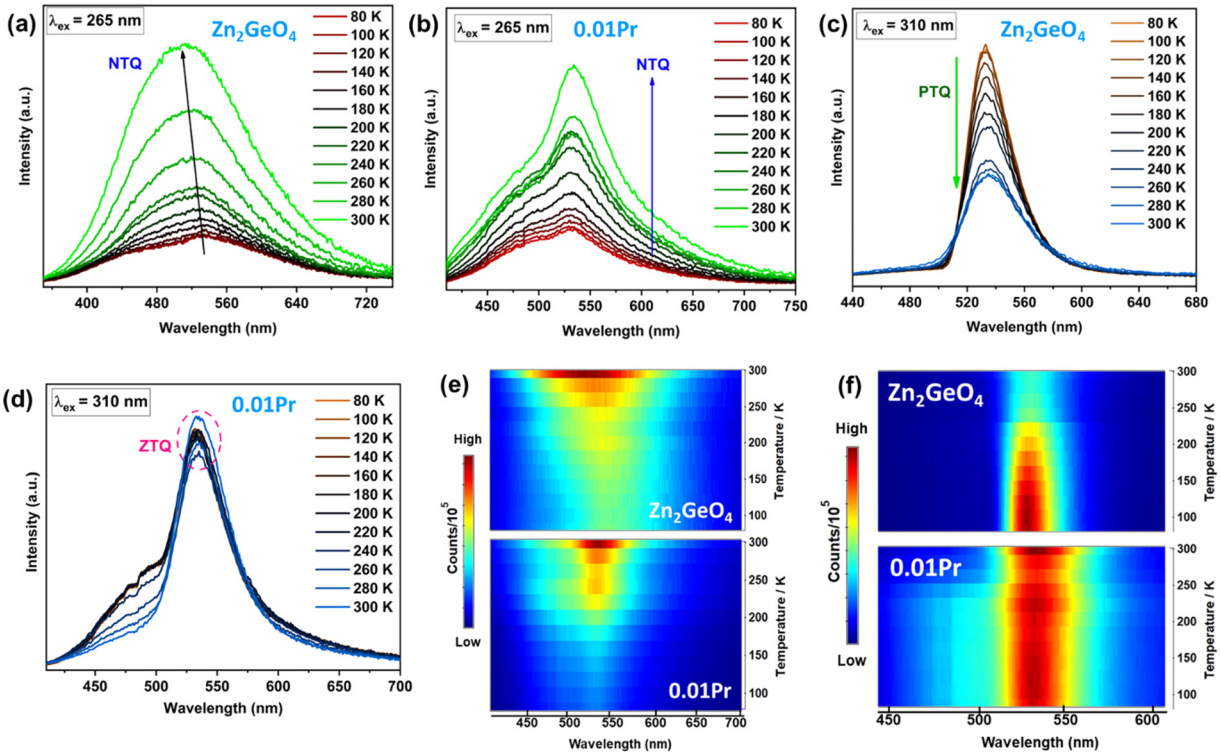


Fig. 6 (a) and (b) Temperature-dependent PL spectra in the range of 80–300 K under 265 nm excitation for $Zn_2GeO_4$ and 0.01Pr samples, respectively. (c) and (d) Temperature-dependent PL spectra in the range of 80–300 K under 310 nm excitation for undoped and Pr doped samples, respectively. (e) and (f) Contour plots demonstrating the intensity variation with temperature for undoped and Pr doped samples at 265 and 310 nm excitations, respectively.

the intensity observed at 80 K (Fig. S30, ESI†). In contrast, the green band intensity of $Zn_2GeO_4$ in the absence of $Pr^{3+}$ doping diminished to 64% of the initial intensity at 80 K.

The main transitions for the relaxations of photo-generated carriers ($e^-$ and $h^+$) between the bandgap and trap states are schematically shown in Fig. 7a. The recombinations from CB have been excluded to understand the dynamics of only defect-mediated PL due to DAP recombinations. The different transitions are:[9,41,57,58] (1) non-radiative capture of electrons by traps, (2) thermal excitation of electrons from traps, (3) thermal excitation of holes from VB, (4) non-radiative capture of holes by VB, (5) tunnel transitions of carriers and relaxations from non-radiative traps (Trap I and Trap II) to luminescent defect sites, (6) radiative DAP transitions, (7) non-radiative recombination process assisted by phonons, and (8) non-radiative relaxations to killer sites. In addition, the thermal hopping of electrons from acceptor levels to spatially separated trap states induces the generation of holes in the acceptor levels. Hence, the NTQ processes in native defect phosphors could be induced *via* thermally activated hopping mechanisms due to the increased probability of DAP transitions (Fig. 7b).

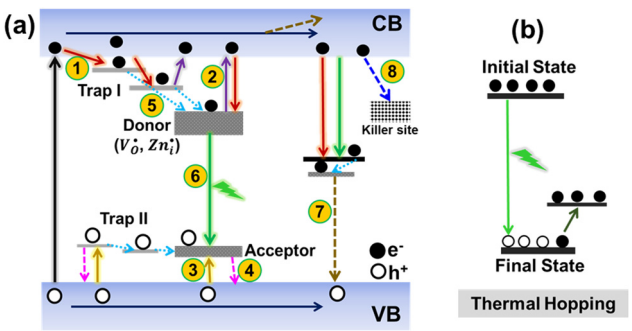


Fig. 7 Schematic illustration of (a) trapping–detrapping processes of photo-generated carriers, and (b) thermal hopping mechanism.

The temperature-dependence studies of luminescence from defect-rich $Zn_2GeO_4$ can reveal the different activation barriers and thermal quenching mechanisms for emissions originating from DAP transitions. The above trapping and detrapping mechanisms are competitive, and the dominance of one over the other in particular temperature zones led to NTQ and PTQ of visible emissions. The temperature dependence of PL in semiconductors with multiple NTQ and PTQ processes has been explained in the literature by Shibata *et al.* by fitting the experimental data in a multi-level model:[59]

$$I_T = I_0 \left( \frac{1 + \sum_{q=1}^{n} A_q \exp(-E_q'/k_B T)}{1 + \sum_{j=1}^{m} B_j \exp(-E_j/k_B T)} \right) \quad (7)$$

where $I_0$ is the initial intensity, $I_T$ is PL the intensity at temperature, $T$ in Kelvin, $k_B$ is the Boltzmann constant, $E_q'$ is

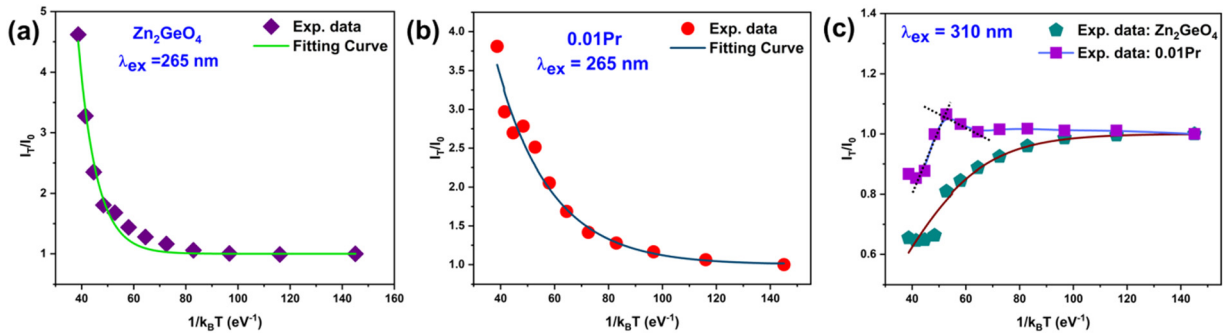


Fig. 8 Ratio of integrated PL intensity ($I_T/I_0$) as a function of $1/k_BT$ for (a) $Zn_2GeO_4$ and (b) $Zn_2GeO_4$ : 0.01$Pr^{3+}$ excited at 265 nm, and (c) undoped and Pr doped $Zn_2GeO_4$ samples excited at 310 nm, respectively.



the activation energy for the $q$-th radiative transition mechanism, and $E_j$ is the activation of $j$-th non-radiative transition, $A_q$ and $B_j$ are constants, $n$ and $m$ are the total number of intermediate radiative and non-radiative processes, respectively. The exponential terms in the numerator and denominator represent a multi-level model for NTQ and PTQ processes, respectively. Fig. 8a, b shows the ratios of integrated PL intensity ($I_T/I_0$) as a function of $1/k_BT$ in the temperature range from 80 to 300 K for $Zn_2GeO_4$ and 0.01Pr samples excited at the bandgap energy (265 nm), respectively. The NTQ of PL emissions under bandgap transitions was best fitted with a single-barrier model with $n = 1$ for $Zn_2GeO_4$ and 0.01Pr samples (eqn (8)). The calculated activation energies are summarized in Table 2.

$$I_T = I_0(1 + A_1 \exp(-E_1'/k_BT) \quad (8)$$

For the NTQ profile of undoped $Zn_2GeO_4$, the calculated activation energy ($E_q'$) is 141 meV. For bandgap excitation, the electrons excited to the CB and holes generated in VB can be captured by shallow and deep traps (Fig. 7a). The calculated barrier height of 141 meV can be explained by the thermal excitation of electrons from trap centres to CB. This process is thermally activated, and hence, the NTQ effect of the PL band can be attributed to enhanced transitions from CB to acceptor levels. This explained the gradual blue shift of PL emission peak in $Zn_2GeO_4$ on increasing the temperature (Fig. 6a). In addition, the increment of holes in acceptor levels by thermally activated excitation of holes from VB to Zn and Ge vacancies will initiate more DAP recombinations. Simultaneously, an increase in temperature may trigger the release of charge carriers from non-radiative defects to luminescent donor sites ($Zn_i^{\bullet}$ and $V_O^{\bullet}$). The above processes dominate over the non-radiative recombinations of charge carriers below RT that may be ascribed to the increased stiffness due to NTE of the $Zn_2GeO_4$ lattice up to 300 K.[25,26] In 0.01Pr, the small barrier (48 meV) for NTQ that resulted in the enhanced PL intensity with temperature indicated the contribution from trap-to-trap tunnelling of charge carriers.[41,47,49,60] Notably, the activation barrier for NTE in 0.01Pr is lower compared to the undoped sample, which can be attributed to improved structural rigidity on $Pr^{3+}$ doping indicated by Raman spectroscopy. The decay kinetic studies by TRES measurements also suggested the prominent role of indirect tunneling pathways for populating the radiative trap states in $Pr^{3+}$ doped samples.

Table 2 Energies for different NTQ and PTQ processes for undoped and Pr-doped $Zn_2GeO_4$ samples

| | NTQ | PTQ |
|---|---|---|
| Sample ($\lambda_{ex}$) | $E'_1$ (meV) | $E_1$ (meV) |
| $Zn_2GeO_4$ (265 nm) | 141 | — |
| $Zn_2GeO_4$ (310 nm) | — | 68 |
| 0.01Pr (265 nm) | 48 | — |
| 0.01Pr (310 nm) | 4 | 17 |

Fig. 8c displays the $I_T/I_0$ as a function of $1/k_BT$ in the temperature range from 80 to 300 K for $Zn_2GeO_4$ and 0.01Pr samples excited at below bandgap energy (310 nm). The PL intensity remained almost constant for $T < 120$ K and above 120 K, and a strong PTQ of the $Zn_2GeO_4$ emission band was observed under below-bandgap NUV excitations. The PTQ process can be modeled by using the expression with a single non-radiative process as below:[61,62]

$$I_T = I_0/(1 + A \exp(-E_1/k_BT)) \quad (9)$$

The activation energy of the TQ process of $Zn_2GeO_4$ emissions is 68 meV and this can be attributed to non-radiative relaxations when charge carriers have enough energy for cross-over due to thermal activation.[56,61] In contrast, for the 0.01Pr sample, the PL intensity remained constant up to 180 K and then increased gradually, showing a weak NTQ effect. After $T > 220$ K, the PL intensity decreased abruptly due to PTQ processes. The activation energies of each component were obtained by fitting the data into eqn (7) with n and $m = 1$, and calculating the slope values after valid approximations proposed by Shibata *et al.*[59] The lower activation energies for NTQ (4 meV) suggested the prominent role of thermal hopping pathways (Fig. 7b) for generating sufficient holes for DAP transitions in $Pr^{3+}$ doped samples. The activation energy for the PTQ (17 meV) process is the barrier for non-radiative relaxations of charge carriers to killer sites. A higher barrier for TQ may be observed at higher temperatures due to the involvement of thermal ionization processes from deep traps.

 

To study the behavior of the bluish-white emission band of undoped $Zn_2GeO_4$ and green emission band of 0.01Pr samples on heating the samples above RT, the temperature-dependent PL spectra for $Zn_2GeO_4$ and 0.01Pr samples were recorded in the range of 298–408 K (Fig. 9a and c). Above RT, the PL intensity decreased on heating, which revealed positive thermal quenching (PTQ) of bluish-white emission. The TQ is observed due to the increased non-radiative charge carrier recombinations, which can be assisted by positive thermal expansion (PTE) of the $Zn_2GeO_4$ lattice above RT which was confirmed by high-temperature XRD studies.

The resistance of $Zn_2GeO_4$ to TQ can be evaluated by using the Arrhenius expression:

$$I_T = I_0/(1 + A\exp(-E_a/kT)) \quad (10)$$

where $I_0$ and $I_T$ denote the PL emission intensity at the initial temperature ($T_0$) and given temperature ($T$), $E_a$ is the activation energy, A represents a constant specific to the host, and $k$ is the Boltzmann constant, respectively. The $E_a$ was calculated from the $\ln(I_0/I_T - 1)$ *versus* the $1/kT$ plot after a linear fitting of the experimental data. From Fig. 9b, two linear sections were observed, and hence, two different $E_a$ values (0.424 eV and 0.139 eV) were obtained in different temperature ranges. This revealed that different thermal processes are dominant at different temperature zones. At lower temperatures, higher activation energy is a result of thermal excitations of charge carriers from deep traps to emissive donor levels and CB, which can compensate for large TQ. However, the TQ processes like thermal ionization and crossover dominate at higher temperatures due to a significant increase in non-radiative vibrational relaxations.[39,61] The activation energy of 0.36 eV for the 0.01Pr sample suggested good thermal stability of the green PL band for the 0.01Pr sample (Fig. 9d) in the temperature range of 358–398 K.

### 2.7. LED application

The LED fabrication was performed to demonstrate the potential of our phosphor material for solid state lighting applications. Fig. 10(a and b) show the electroluminescence (EL) spectra of undoped and $Pr^{3+}$ doped $Zn_2GeO_4$ samples using 280 nm LED chips. The performance of pc-LED was evaluated, and the parameters for pc-LED are presented in Table 3. A crucial point to be noted is that the CRI value is slightly reduced in the case of the $0.01Pr^{3+}$-doped phosphor-based LED compared to that of the undoped one. This is reasonable since the emission peak of the $0.01Pr^{3+}$-doped sample slightly shifted towards the higher wavelength side and has narrower emission width compared to that of the undoped sample, as shown in the normalized emission spectral comparison (Fig. 3b), and in the EL spectral comparison (Fig. S31, ESI†). The reason for this has been discussed in the photoluminescence section of this manuscript. Because of such red shifting and narrowing of the emission width, the emission curve of the $Pr^{3+}$-doped sample covered a

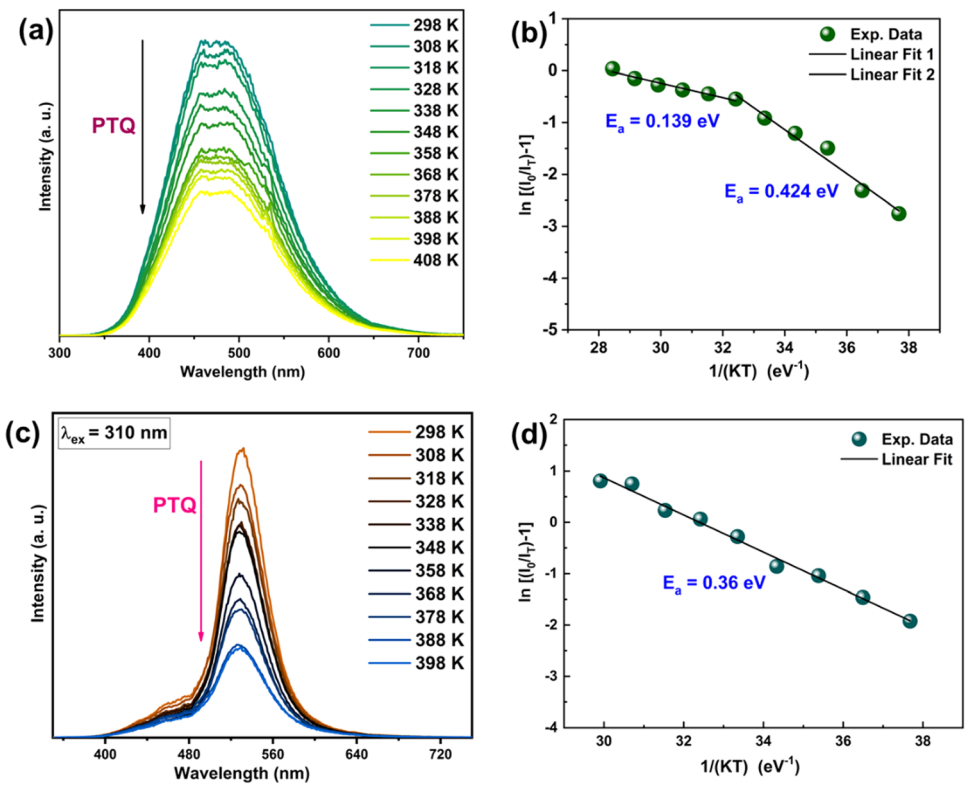


Fig. 9 Temperature-dependent PL spectra for the $Zn_2GeO_4$ sample in the range of 298–408 K under excitation at (a) 265 nm. (b) $\ln(I_0/I_T - 1)$ *versus* $1/kT$ for the $Zn_2GeO_4$ phosphor. (c) Temperature-dependent PL spectra for the 0.01Pr sample in the range of 298–408 K under excitation at 310 nm, and (d) $\ln(I_0/I_T - 1)$ *versus* $1/kT$ for the 0.01Pr phosphor.

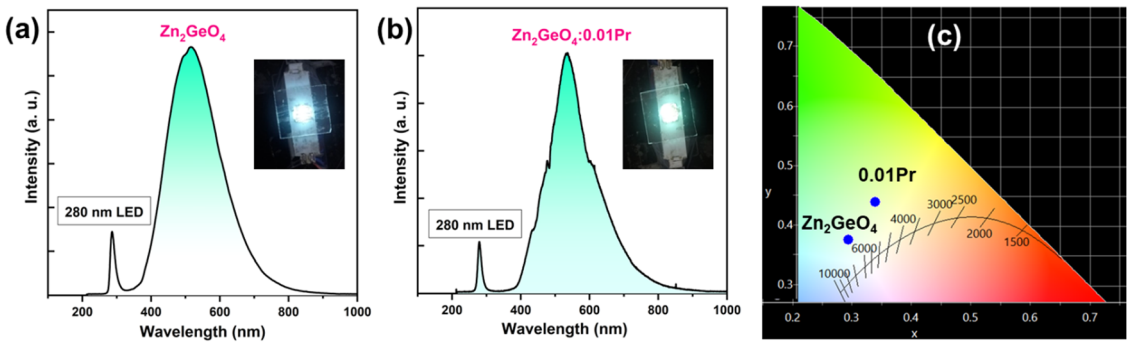


Fig. 10 EL spectra of (a) undoped and (b) $Pr^{3+}$ doped $Zn_2GeO_4$ on 280 nm LED excitation, and (c) the CIE color coordinate diagram.

Table 3 CIE color coordinates, CRI and CCT values for undoped and $Pr^{3+}$ doped $Zn_2GeO_4$

| Samples | CIE | CRI | CCT |
|---|---|---|---|
| $Zn_2GeO_4$ | (0.2940, 0.3765) | 76 | 7004 |
| $Zn_2GeO_4$:0.01Pr | (0.3315, 0.4393) | 72 | 5546 |

lower visible region compared to the emission curve of the undoped sample. That is the main reason why the $Pr^{3+}$ doped sample showed a slightly lower CRI compared to that of the undoped sample. The respective color coordinates of EL obtained in both the phosphors are marked in the color coordinate diagram (Fig. 10c). Moreover, the phosphors exhibiting long afterglow decay times (in ms) can be promising for pc- LED to compensate for the dimming time and flicker effects.[63] The potential application of $Zn_2GeO_4$ and 0.01Pr phosphors in solid-state lighting can be supported by high color rendering index (CRI) and correlated color temperature (CCT) values. The optimum CCT for daylight and CRI values were obtained in the 0.01Pr sample. Hence, trap tuning in $Zn_2GeO_4$ can be a promising approach for developing bluish-white and green-emitting phosphors for warm pc-LED applications.

## 3. Conclusion

Here, detailed studies of NTE in the $Zn_2GeO_4$ phosphor and luminescent properties have been carried out to understand the optical response of self-activated $Zn_2GeO_4$. A doping strategy of hypervalent $Pr^{3+}$ was employed to realize controllable trap tuning, defect-related trap depths, and improved PLQY with long afterglow. The decay kinetics of visible emissions was studied by time-resolved fluorescence spectroscopy (TRES) to understand the photophysics of complex PL emissions of $Zn_2GeO_4$. This knowledge is crucial for optimum trap tuning and improving the PLQY and PersL performance by solving the afterglow mechanisms. Interestingly, a spectral shift from blue to green was observed in the emission spectra within different time windows. A two-fold enhancement in PLQY of green emission was achieved on $Pr^{3+}$ doping. Importantly, the $Pr^{3+}$ doping increased shallow traps that facilitated efficient PersL at RT. The existence of trap-to-trap tunnelling mechanisms imparts longer afterglow decay lifetimes, as confirmed by fitting into the power-law decay function. The $Pr^{3+}$ doped $Zn_2GeO_4$ phosphor demonstrated a long X-ray-activated PersL at room temperature for up to 18 hours. The thermal behavior of the emission band at bandgap and below bandgap energies was investigated extensively to reveal the different trapping–detrapping processes. The LED fabrication was performed to display the electroluminescent spectrum of phosphors, and the trap tuning in $Zn_2GeO_4$ can be a promising strategy for developing warm pc-LEDs.

## Data availability

All data required to reproduce the results in the paper are available in main text and the ESI.†

## Conflicts of interest

There are no conflicts to declare.

## Acknowledgements

A. Balhara and S.K. Gupta would like to acknowledge Apurav Guleria, RPCD for Raman measurements, N. Rawat for TL measurements, Kathi Sudarshan, RCD for help in Rietveld analysis, Dr Ruma Gupta for EDAX and elemental mapping, Dr Manoj Mohapatra for EPR measurements, Dr Dibyendu Bhattacharyya and Dr Biplab Ghosh for help in getting EXAFS beamline, Dr Rohan Phatak for high temperature XRD, and Dr Aviru Kumar Basu, INST for XPS measurements. We acknowledge Dr P S Sarkar, TPD, for providing an X-ray tube and Dr Meghnath Sen, RSSD, for TL measurements on X-ray irradiated samples. This work was funded by Bhabha Atomic Research Centre (BARC) which is a government of India funded research institute.

## References

1 J. Zhang, Z. Song, P. Cai and X. Wang, Structures, photoluminescence, and principles of self-activated phosphors, *Phys. Chem. Chem. Phys.*, 2023, **25**(3), 1565–1587.



 

2 N. Pathak, P. S. Ghosh, S. K. Gupta, S. Mukherjee, R. M. Kadam and A. Arya, An Insight into the Various Defects-Induced Emission in $MgAl_2O_4$ and Their Tunability with Phase Behavior: Combined Experimental and Theoretical Approach, *J. Phys. Chem. C*, 2016, **120**(7), 4016–4031.
3 Y. Shi, X. Zhang, X. Chen and Y. Zhang, Trap-tuning in afterglow perovskite crystals through alkali metal ion doping, *Chem. Commun.*, 2022, **58**(72), 10048–10051.
4 J. Zhou, G. Zheng, X. Liu, G. Dong and J. Qiu, Defect engineering in lanthanide doped luminescent materials, *Coord. Chem. Rev.*, 2021, **448**, 214178.
5 F. Gao, Q. Pang, D. Gao, C. Jia, H. Xin, Y. Pan, Y. Wang and S. Yun, $Mn^{2+}$-Activated Photostimulable Persistent Nanophosphors by $Pr^{3+}$ Codoping for Rewritable Information Storage, *ACS Appl. Nano Mater.*, 2023, **6**(4), 3054–3064.
6 C. Guo, K. Tian, L. Wang, F. Liang, F. Wang, D. Chen, J. Ning, Y. Zhong and Y. Hu, Approach of Fermi level and electron-trap level in cadmium sulfide nanorods via molybdenum doping with enhanced carrier separation for boosted photocatalytic hydrogen production, *J. Colloid Interface Sci.*, 2021, **583**, 661–671.
7 Y. Kuang, Y. Li, B. Chen, S. Zhao, M. Chen, S. Lian and J. Zhang, Regulating anti-thermal quenching to zero thermal quenching for highly efficient blue-emitting Eu2+-doped K-beta-alumina phosphors, *J. Mater. Chem. C*, 2023, **11**(17), 5874–5881.
8 Y. Xu, Z. Zhou, P. Yu and Y. Wang, Al-doped CuS/$Znln_2S_4$ forming Schottky Junction Induced Electron Trap Centers for Photocatalytic Overall Water Splitting, *Chem. Eng. J.*, 2023, 144275.
9 Y. Chen, B. Yu, J. Gou and S. F. Liu, Zero-thermal-quenching and photoluminescence tuning with the assistance of carriers from defect cluster traps, *J. Mater. Chem. C*, 2018, **6**(40), 10687–10692.
10 K. Huang, N. Le, J. S. Wang, L. Huang, L. Zeng, W. C. Xu, Z. Li, Y. Li and G. Han, Designing next generation of persistent luminescence: recent advances in uniform persistent luminescence nanoparticles, *Adv. Mater.*, 2022, **34**(14), 2107962.
11 Y. Li, M. Gecevicius and J. Qiu, Long persistent phosphors—from fundamentals to applications, *Chem. Soc. Rev.*, 2016, **45**(8), 2090–2136.
12 X. Wang, X. Zhang, S. Yan, H. Liu and Y. Zhang, Nearly-Unity Quantum Yield and 12-Hour Afterglow from a Transparent Perovskite of $Cs_2NaScCl_6$:Tb, *Angew. Chem., Int. Ed.*, 2022, **61**(40), e202210853.
13 S. Wang, Z. Song and Q. Liu, Recent progress in Ce3+/Eu2+-activated LEDs and persistent phosphors: focusing on the local structure and the electronic structure, *J. Mater. Chem. C*, 2023, **11**, 48–96.
14 H. Miao, Y. Zhou, P. Wang, Z. Huang, W. Zhaxi, L. Liu, F. Duan, J. Wang, X. Ma and S. Jiang, High-temperature negative thermal quenching phosphors from molecular-based materials, *Chem. Commun.*, 2023, **59**(9), 1229–1232.
15 H. Yuan, Q. Gao, P. Xu, J. Guo, L. He, A. Sanson, M. Chao and E. Liang, Understanding negative thermal expansion of $Zn_2GeO_4$ through local structure and vibrational dynamics, *Inorg. Chem.*, 2021, **60**(3), 1499–1505.
16 J. Dolado, F. Malato, J. Segura-Ruiz, R. Martínez-Casado, M. Taeño, I. Snigireva, P. Hidalgo, B. Méndez and G. Martínez-Criado, Interplay between Crystal Structure and Optical Response in Plateau–Rayleigh $Zn_2GeO_4/SnO_2$ Heterostructures, *Adv. Photonics Res.*, 2023, **4**(8), 2300063.
17 X. Li, Y. Feng, M. Li, W. Li, H. Wei and D. Song, Smart hybrids of $Zn_2GeO_4$ nanoparticles and ultrathin g-$C_3N_4$ layers: synergistic lithium storage and excellent electrochemical performance, *Adv. Funct. Mater.*, 2015, **25**(44), 6858–6866.
18 Z. Ma, X. Liu, X. Wang, Z. Luo, W. Li, Y. Nie, L. Pei, Q. Mao, X. Wen and J. Zhong, Manipulating the d-band center enhances photoreduction of $CO_2$ to CO in $Zn_2GeO_4$ nanorods, *Chem. Eng. J.*, 2023, **468**, 143569.
19 S. Yan, L. Wan, Z. Li and Z. Zou, Facile temperature-controlled synthesis of hexagonal $Zn_2GeO_4$ nanorods with different aspect ratios toward improved photocatalytic activity for overall water splitting and photoreduction of $CO_2$, *Chem. Commun.*, 2011, **47**(19), 5632–5634.
20 H. Zhao, X. Wang, J. Feng, Y. Chen, X. Yang, S. Gao and R. Cao, Synthesis and characterization of $Zn_2GeO_4$/Mg-MOF-74 composites with enhanced photocatalytic activity for $CO_2$ reduction, *Catal. Sci. Technol.*, 2018, **8**(5), 1288–1295.
21 J. Dolado, J. García-Fernández, P. Hidalgo, J. González-Calbet, J. Ramírez-Castellanos and B. Méndez, Intense cold-white emission due to native defects in $Zn_2GeO_4$ nanocrystals, *J. Alloys Compd.*, 2022, **898**, 162993.
22 J. Dolado, B. Rodríguez, R. Martínez-Casado, I. Píš, E. Magnano, P. Hidalgo and B. Méndez, Li-doping effects on the native defects and luminescence of $Zn_2GeO_4$ microstructures: Negative thermal quenching, *Acta Mater.*, 2023, **245**, 118606.
23 S. K. Gupta, K. Sudarshan, B. Modak and R. Gupta, Interstitial Zinc Boosted Light Tunability, Afterglow, and Ultrabright White Emission in Zinc Germanate ($Zn_2GeO_4$), *ACS Appl. Electron. Mater.*, 2023, **5**(2), 1286–1294.
24 G. Gao, M. Peng and L. Wondraczek, Spectral shifting and NIR down-conversion in Bi3+/Yb3+ co-doped Zn2GeO4, *J. Mater. Chem. C*, 2014, **2**(38), 8083–8088.
25 G. Liu, M. S. Molokeev and Z. Xia, Structural rigidity control toward Cr3+-based broadband near-infrared luminescence with enhanced thermal stability, *Chem. Mater.*, 2022, **34**(3), 1376–1384.
26 Y. Wei, H. Yang, Z. Gao, X. Yun, G. Xing, C. Zhou and G. Li, Anti-Thermal-Quenching Bi3+ Luminescence in a Cyan-Emitting Ba2ZnGe2O7:Bi Phosphor Based on Zinc Vacancy, *Laser Photonics Rev.*, 2021, **15**(1), 2000048.
27 R. M. Calderón-Olvera, E. Arroyo, A. M. Jankelow, R. Bashir, E. Valera, M. Ocaña and A. I. Becerro, Persistent Luminescence Zn2GeO4:Mn2+ Nanoparticles Functionalized with Polyacrylic Acid: One-Pot Synthesis and Biosensing Applications, *ACS Appl. Mater. Interfaces*, 2023, **15**(17), 20613–20624.
28 D. Gao, F. Gao, Q. Kuang, X. Zhang, Z. Zhang, Y. Pan, R. Chai and H. Jiao, Zinc Germanate nanophosphors with persistent luminescence for multi-mode imaging of latent fingerprints, *ACS Appl. Nano Mater.*, 2022, **5**(7), 9929–9939.

29 B. B. Srivastava, S. K. Gupta, Y. Li and Y. Mao, Bright persistent green emitting water-dispersible $Zn_2GeO_4$:Mn nanorods, *Dalton Trans.*, 2020, **49**(22), 7328–7340.
30 X. Wang and Y. Mao, Recent advances in Pr3+-activated persistent phosphors, *J. Mater. Chem. C*, 2022, **10**(10), 3626–3646.
31 M. Wan, Y. Wang, X. Wang, H. Zhao and Z. Hu, The properties of a novel green long afterglow phosphor Zn2GeO4:Mn2+,Pr3+, *Opt. Mater.*, 2014, **36**(3), 650–654.
32 M. Anenburg, A. D. Burnham and J. L. Hamilton, Quadrivalent praseodymium in planetary materials, *Am. Mineral.*, 2020, **105**(12), 1802–1811.
33 V. Sadykov, N. Eremeev, Z. Vinokurov, A. Shmakov, V. Kriventsov, A. Lukashevich, A. Krasnov and A. Ishchenko, Structural studies of pr nickelate-cobaltite-Y-doped ceria nanocomposite, *J. Ceram. Sci. Technol.*, 2017, **8**(1), 129–140.
34 J. Dolado, R. Martínez-Casado, P. Hidalgo, R. Gutierrez, A. Dianat, G. Cuniberti, F. Domínguez-Adame, E. Díaz and B. Méndez, Understanding the UV luminescence of zinc germanate: The role of native defects, *Acta Mater.*, 2020, **196**, 626–634.
35 H. He, Y. Zhang, Q. Pan, G. Wu, G. Dong and J. Qiu, Controllable synthesis of $Zn_2GeO_4$:Eu nanocrystals with multi-color emission for white light-emitting diodes, *J. Mater. Chem. C*, 2015, **3**(21), 5419–5429.
36 J. Dolado, P. Hidalgo and B. Méndez, Correlative study of vibrational and luminescence properties of Zn2GeO4 microrods, *Phys. Status Solidi A*, 2018, **215**(19), 1800270.
37 P. Hidalgo, A. López, B. Méndez and J. Piqueras, Synthesis and optical properties of $Zn_2GeO_4$ microrods, *Acta Mater.*, 2016, **104**, 84–90.
38 Z. Liu, X. Jing and L. Wang, Luminescence of native defects in $Zn_2GeO_4$, *J. Electrochem. Soc.*, 2007, **154**(6), H500.
39 X. Chen, X. Wu, L. Yue, L. Zhu, W. Pan, Z. Qi, S. Wang and J. Shao, Negative thermal quenching of below-bandgap photoluminescence in InPBi, *Appl. Phys. Lett.*, 2017, **110**, 5.
40 D. Kulesza, A. J. Bos and E. Zych, The effect of temperature and excitation energy of the high-and low-spin 4f→ 5d transitions on charging of traps in $Lu_2O_3$:Tb,M (M = Ti,Hf), *Acta Mater.*, 2022, **231**, 117852.
41 X. Wang, Z. Feng, J. Shi, G. Jia, S. Shen, J. Zhou and C. Li, Trap states and carrier dynamics of $TiO_2$ studied by photoluminescence spectroscopy under weak excitation condition, *Phys. Chem. Chem. Phys.*, 2010, **12**(26), 7083–7090.
42 J. Ren, X. Xu, H. Zeng, G. Chen, D. Kong, C. Gu, C. Chen, Z. Liu and L. Kong, Novel Self-Activated Zinc Gallogermanate Phosphor: The Origin of its Photoluminescence, *J. Am. Ceram. Soc.*, 2014, **97**(10), 3197–3201.
43 M. D'Arienzo, M. Redaelli, B. Di Credico, S. Polizzi, R. Scotti and F. Morazzoni, New insights into the sensing mechanism of shape controlled ZnO particles, *RSC Adv.*, 2016, **6**(58), 52987–52997.
44 V. Ischenko, S. Polarz, D. Grote, V. Stavarache, K. Fink and M. Driess, Zinc oxide nanoparticles with defects, *Adv. Funct. Mater.*, 2005, **15**(12), 1945–1954.
45 S. Pramanik, S. Mukherjee, S. Dey, S. Mukherjee, S. Das, T. Ghosh, P. Ghosh, R. Nath and P. K. Kuiri, Cooperative effects of zinc interstitials and oxygen vacancies on violet-blue photoluminescence of ZnO nanoparticles: UV radiation induced enhanced latent fingerprint detection, *J. Lumin.*, 2022, **251**, 119156.
46 D. Savchenko, A. Vasin, O. Kuz, I. Verovsky, A. Prokhorov, A. Nazarov, J. Lančok and E. Kalabukhova, Role of the paramagnetic donor-like defects in the high n-type conductivity of the hydrogenated ZnO microparticles, *Sci. Rep.*, 2020, **10**(1), 17347.
47 J. Kong, W. Zheng, Y. Liu, R. Li, E. Ma, H. Zhu and X. Chen, Persistent luminescence from Eu3+ in SnO2 nanoparticles, *Nanoscale*, 2015, **7**(25), 11048–11054.
48 W. Sun, R. Pang, H. Li, D. Li, L. Jiang, S. Zhang, J. Fu and C. Li, Investigation of a novel color tunable long afterglow phosphor KGaGeO4:Bi3+: luminescence properties and mechanism, *J. Mater. Chem. C*, 2017, **5**(6), 1346–1355.
49 A. Barzykin and M. Tachiya, Mechanism of charge recombination in dye-sensitized nanocrystalline semiconductors: Random flight model, *J. Phys. Chem. B*, 2002, **106**(17), 4356–4363.
50 Y. Zhang, Y. Liang, X. Shan, D. Chen, S. Miao, R. Shi, F. Xie and W. Wang, X-ray-Excited Long-Lasting Narrowband Ultraviolet-B Persistent Luminescence from Gd3+-Doped Sr2P2O7 Phosphor, *Inorg. Chem.*, 2022, **61**(50), 20647–20656.
51 H. Suo, X. Zhang and F. Wang, Controlling X-ray-activated persistent luminescence for emerging applications, *Trends Chem.*, 2022, **4**(8), 726–738.
52 C. Richard and B. Viana, Persistent X-ray-activated phosphors: mechanisms and applications, *Light: Sci. Appl.*, 2022, **11**(1), 123.
53 S. Ge, H. Peng, Q. Wei, X. Shen, W. Huang, W. Liang, J. Zhao and B. Zou, Realizing Color-Tunable and Time-Dependent Ultralong Afterglow Emission in Antimony-Doped $CsCdCl_3$ Metal Halide for Advanced Anti-Counterfeiting and Information Encryption, *Adv. Opt. Mater.*, 2023, 2300323.
54 W. Zheng, X. Li, N. Liu, S. Yan, X. Wang, X. Zhang, Y. Liu, Y. Liang, Y. Zhang and H. Liu, Solution-grown chloride perovskite crystal of red afterglow, *Angew. Chem.*, 2021, **133**(46), 24655–24660.
55 F. Peng, T. Seto and Y. Wang, First Evidence of Electron Trapped Ln2+ Promoting Afterglow on Eu2+, Ln3+ Activated Persistent Phosphor-Example of BaZrSi3O9: Eu2 +, Sm3 +, *Adv. Funct. Mater.*, 2023, 2300721.
56 Y.-C. Lin, M. Bettinelli and M. Karlsson, Unraveling the mechanisms of thermal quenching of luminescence in Ce3+-doped garnet phosphors, *Chem. Mater.*, 2019, **31**(11), 3851–3862.
57 M. A. Reshchikov, Two-step thermal quenching of photoluminescence in Zn-doped GaN, *Phys. Rev. B: Condens. Matter Mater. Phys.*, 2012, **85**(24), 245203.
58 A. J. van Bunningen, A. D. Sontakke, R. van der Vliet, V. G. Spit and A. Meijerink, Luminescence Temperature Quenching in Mn2+ Phosphors, *Adv. Opt. Mater.*, 2023, **11**(6), 2202794.
59 H. Shibata, Negative thermal quenching curves in photoluminescence of solids, *Jpn. J. Appl. Phys.*, 1998, **37**(2R), 550.

 

60 D. Huntley, An explanation of the power-law decay of luminescence, *J. Phys.: Condens. Matter*, 2006, **18**(4), 1359.
61 J. Dolado, P. Hidalgo and B. Méndez, Kinetic Study of the Thermal Quenching of the Ultraviolet Emission in Zn2GeO4 Microrods, *Phys. Status Solidi RRL*, 2022, **16**(6), 2100613.
62 J. J. Joos, D. Van der Heggen, L. I. Martin, L. Amidani, P. F. Smet, Z. Barandiarán and L. Seijo, Broadband infrared LEDs based on europium-to-terbium charge transfer luminescence, *Nat. Commun.*, 2020, **11**(1), 3647.
63 Y.-F. Liu, P. Liu, L. Wang, C.-E. Cui, H.-C. Jiang and J. Jiang, A two-step solid-state reaction to synthesize the yellow persistent Gd3Al2Ga3O12:Ce3+ phosphor with an enhanced optical performance for AC-LEDs, *Chem. Commun.*, 2017, **53**(77), 10636–10639.